ROMA TRE
UNIVERSITÀ DEGLI STUDI

Università degli Studi Roma Tre

Dottorato in Fisica XX ciclo

KINETICS OF NUCLEATION AND AGGREGATION IN
α-CRYSTALLIN SUSPENSIONS

Chairperson	Supervisor(s)
of the Ph.D. School	prof. G. Arcovito
prof. G. Altarelli	prof.ssa M.A. Ricci

Giuseppe Maulucci

A.A. 2007

Index

1.Introduction

1.1.   Cataract

The eye and its architecture, at the macroscopic, microscopic and molecular level, is a nature's masterpiece. Most impressive is the optical quality of the lens: the cones in the retina are visible through the intact optics of animal and human eyes (Hughes, 1996). The lens is a cellular organ and its transparency is due to its complex architecture and unique protein composition. Unfortunately, the delicate balance required for transparency is easily disturbed with lens opacity, cataract, as a result.

Cataract is the most common cause of blindness, and, therefore, of enormous medical and economical relevance worldwide. Ultimately, the only way to restore sight is cataract surgery. Current levels of surgery remain too low to tackle the backlog of cataract blind, estimated to be 16–20 million worldwide, and to reduce the rising world incidence due to the ageing population. The social impact and economic cost of cataract have motivated extensive research on the lens and an enormous amount of knowledge has been accumulated.

From the physicochemical point of view, the main cause for lens opacification is the condensation of eye lens proteins into *randomly distributed aggregates* with

average molecular masses beyond 50 MDa (Benedek, 1971, 1997). Unfortunately, the main cause of protein lens aggregation is still unknown. The causes of aggregation can be several: point mutations, disulfide bond formation, post-translational modifications leading to altered protein interactions, like deamidation and methylation (Hleon et al., 1999; Kmoch et al., 2000). An increasing number of diseases are believed to result from the aggregation of *misfolded* proteins: a failure in the physical process by which a polypeptide folds into its characteristic three-dimensional structure (*protein folding*), usually produces proteins with altered interactions that can lead to their multimerization into insoluble, extracellular aggregates and/or intracellular inclusions (Carrel, 1997; Dobson, 1999; Soto, 2001). Among these protein-misfolding diseases there are the Alzheimer's disease (AD), Parkinson's disease (PD), Huntington's disease (HD) (and related polyglutamine disorders including several forms of spinocerebellar ataxia or SCA), transmissible spongiform encephalopathies (TSEs, which include several human and animal diseases) and amyotrophic lateral sclerosis (ALS). Despite their obvious differences in clinical symptoms and disease progression, they share some common features: kinetic studies have shown that the aggregation of Aβ, PrP, huntingtin, α-synuclein and other proteins involved in these diseases follows a nucleation mechanism (Jarret, 1993; Scherzinger, 1999; Wood, 1999) which resembles a crystallization process. The critical event is the formation of protein oligomers that act as a nucleus to direct further growth of aggregates. Nucleation-dependent aggregation is characterized by a slow lag phase in which a series of unfavourable interactions forms an oligomeric nucleus, which then rapidly grows to form larger polymers. The lag phase can be minimized or removed by addition of seeds (Dobson, 1999). Several studies showed how cataract could be considered among the protein misfolding diseases because, in stressful conditions, heat and Ca^{2+} decrease both secondary and tertiary–quaternary structure stability of the lenticular structural protein α–*crystallin*, having the

effect of a partial unfolding (Del Valle, 2001). But detailed characterizations of lens proteins aggregation kinetics are still lacking, although they are an important tool to distinguish whether cataract can be considered among the protein misfolding diseases, or among diseases involving altered protein interactions with native proteins.

Another important aspect being debated pertains the main cause of misfolding diseases. Environmental factors that might catalyse protein misfolding and the related pathologies include changes in ions like Ca^{2+}, pH or oxidative stress, thermal stress, macromolecular crowding and increases in the concentration of the misfolded protein (Teplow, 1998). Among these, the prevalent hypothesis for protein folding diseases is that they result from an insufficiency in the protein *chaperoning* system of the cell: to ensure that cells and organisms function properly, the unfolding of cytoplasmic proteins evokes stress induced systems (*heat shock responses*) that inhibit general protein synthesis, and switch the resources of the cell to synthesizing protein chaperones, thus giving cells time and means to deal with the unfolded protein stress. The disease starts when the unfolded protein accumulates faster than the chaperoning system can deal with aggregating protein (Dobson, 1999; Csermely, 2001). It should be noted that among the most prominent cytoplasmic chaperones synthesized, like Hsp90, Hsp70 and the *small heat shock proteins* (sHsps), there is also α−crystallin. This should have an important protective role, because the lens cell lacks protein synthetic capacity and thus cannot increase its protein chaperone content when non-native protein starts aggregating. Therefore, in analogy with the protein misfolding diseases, the main cause for cataract could be that, with time, as lenticular proteins unfold, the chaperone capacity of α−crystallin will be exhausted and protein aggregates will be formed (Horwitz, 1992; Derham and Harding, 1999; Clark and Muchowski, 2000). Investigations on aggregation kinetics of α-crystallins in hyperthermic

and stressful conditions can be a valuable tool in searching if a protective mechanism exists, how it works, why and when it ceases to work .

1.2 Aim of this work

We have seen how a detailed characterization of the aggregation kinetics of the lens proteins allows to distinguish among the different molecular mechanisms responsible for their condensation.

Therefore, in this thesis we will report the aggregation kinetics of the lens structural protein α-crystallin followed *in vitro,* under physiological and paraphysiological conditions. Next, we will develop a quantitative kinetic model of the process that leads to the condensation of eye lens proteins into randomly distributed aggregates by means of population balance equations (PBE), combined with an extensive experimental investigation using light scattering in order to compute experimentally measured quantities.

The model describes the growth kinetics as a two step-process, a nucleation phase followed by an aggregation phase. This mechanism is a further evidence that cataract can be considered among the protein misfolding disease and is not an aggregation process due to altered native protein interactions.

Furthermore, for the first time we will verify how condensation of misfolded proteins does lead also to randomly distributed aggregates, and not only to fibrillization, through a nucleation mechanism, as hipotized by Dobson (Dobson, 1999). This means that nucleation, rather than fibrillization, is a common feature of the misfolding diseases.

Last, but not least, we will find evidence that the α-crystallin exhibits a temperature-dependent protective effect towards self-aggregation, which preserves the lens from a premature opacification by delaying the aggregation of denatured crystallins in hypertermic and stressful conditions. A possible mechanism explaining this effect will be given on the basis of the available

experimental data. This peculiar response to external insults it has been investigated *in vitro* and it could be directly related to the response expressed *in vivo*, because the lens fibre cell represents a special case of aged cells, characterized by a complete lack of an heat shock system except for one component, α-crystallin.

2. Structure of crystallins

2.1 Lens differentiation: structuring a tissue for transparency

The lens is a focusing device that allows images to be formed on the retina. To serve this function, the eye lens has to fulfil two requirements; it has to provide transparency and a high refractive index, i.e. low light scattering and high solubility of its cytoplasmic proteins, the crystallins. From the physical point of view, transparency is limited by absorption and scattering of visible light. In the cataract-free lens, absorption in the visible wavelength range is negligible. The cellular structure of the lens can meet these biophysical requirements because of its unique morphology and composition. In the mature lens, hexagonally packed, long ribbon-like fibre cells, which in man are up to 10 mm long, are arranged in concentric shells, with the oldest cells at the centre and the youngest on the outside (Fig. 1). The shape of the fibre cells is determined and maintained by an extensive cytoskeleton. The lens fibre cells have an unusually high protein content: the soft ovoid human lens has a protein concentration around 0.32 g/ml. The abundant water-soluble crystallins account for most of the lens fibre cell protein.

Light scattering may originate from the differing refractive indices of the membrane and the cytoplasm of the fibre cells, particularly in the cortex (Michael et al., 2003). The experimental evidence for this refractive index difference is clearly seen in the diffraction peaks recorded when laser light is passed through a thin peripheral section of the lens (Benedek, 1979). The absence of diffraction when light is directed along the optical axis is presumably a consequence of the continuous gradual change in orientation between layers of cells along this axis. In the centre of the lens, the refractive index of the membranes is the same as that of the cytoplasm and the orientation of the membrane is of lesser importance (Michael et al., 2003). The lens is determined during early embryonic development (Grainger, 1992) and derives from the ectoderm overlaying the optic cup. The surface ectoderm cells invaginate to form the lens vesicle with cells on the posterior side elongating to primary lens fibre cells filling the vesicle space. Cells on the anterior side remain a monolayer of epithelial cells, with their basal side facing outward and the apical side facing towards the lens fibre cells (Fig. 1).
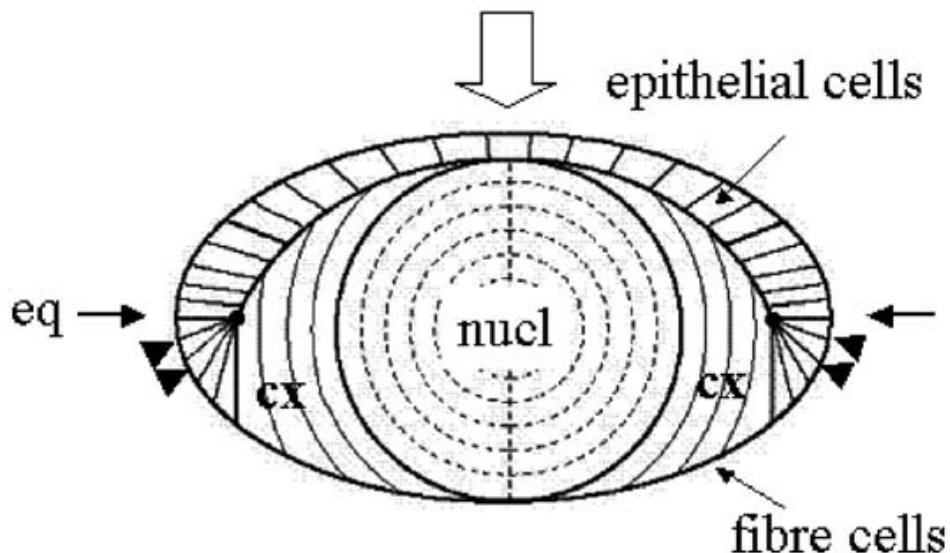
FIGURE 1. Schematic drawing of a sagittal section through a vertebrate lens. The monolayer of epithelial cells and the fibre cell mass are indicated. The direction of incident light and the optical axis is represented by the open arrow; the equatorial plane by the two single arrows. The arrowheads show the region where the epithelial cells differentiate to secondary fibre cells. nucl: the nuclear region; cx: the cortical region, eq: the equatorial region.

Lens epithelial cells divide in a region just anterior to the equator, the cells at the equatorial zone elongate to form secondary fibre cells which form a continuous layer overlaying the primary fibres (Bron, 2000). During differentiation of the fibre cells, the different classes of crystallin genes are expressed in a strict temporal and spatial order. Furthermore, the expression of the crystallin genes is regulated in a developmental manner, with some of the crystallins being expressed primarily in the foetal lens, others only later. Crystallins synthesized during early development will be located in the core of the mature lens; crystallins expressed during later development will abound in the cortex. The design principle of vertebrate lenses is thus one of deposition of complex mixtures of crystallins that vary in their relative proportions along the optical axis and the equatorial plane, put in place by differential gene activity during development. As the last step in differentiation, fibre cells lose their nuclei, mitochondria and ribosomes in a process resembling the early steps of apoptosis (Bassnett, 2002). This loss of cellular organelles is required for transparency but has as consequence that the terminally differentiated fibre cell can no longer synthesize or degrade proteins. Hence, lens proteins that are located at the centre of the lens, and synthesized during foetal development, cannot be replaced and must last for the whole lifetime of the organism.

2.2. The crystallins

The abundant soluble proteins of the vertebrate eye lens are collectively known as the crystallins (Table 1). All vertebrate lenses examined contain three classes of crystallins, the α-, β- and γ-crystallins, also known as the ubiquitous crystallins, although in widely varying ratios. Using a mixture of different sized protein assemblies to fill the lens fibre cells insures polydispersity and prevents crystallization.

In order to fulfil their optical function, crystallins have to be first and foremost soluble. As they have to last the whole life span of the organism they must also be stable.

Table 1
Some crystallin parameters

Crystallin	Residues	Size (kDa)	pI	SwissProt	PDB	MIM
Human lens crystallins						
αA	173	19 909	5.6	P02489	—	123 580
αB	175	20 159	6.8	P02511	—	123 590
βB1	251	27 892	8.6	P53674	1oki	600 929
βB2	204	23 249	6.5	P43320	—	123 620
βB3	211	24 230	5.9	P26998	—	123 630
βA1	198	23 191	6.4	P05813	—	123 610
βA2	196	21 964	5.9	P53672	—	600 836
βA3	215	25 150	5.7	P05813	—	123 610
βA4	195	22 243	5.8	P53673	—	123 631
γS	177	20 875	6.4	P22914	1ha4[a]	123 730
γA	173	20 761	7.8	P11844	—	123 660
γB	174	20 776	7.0	P07316	—	123 670
γC	173	20 747	7.0	P07315	—	123 680
γD	173	20 607	7.2	P07320	1hk0	123 690
Crystallins and homologs with X-ray structures						
Bovine γS	177	20 796		P06504	1a7h[a]	
Bovine γB	174	20 965		P02526	1amm	
Bovine γD	173	20 735		P08209	1elp	
Bovine γE	173	21 008		[b]	1m8u	
Bovine γF	173	20 955		P23005	1a45	
Rat γE	173	21 132		P02528	1a5d	
Rat βB2	204	23 250		P26775	1e7n	
Bovine βB2	204	23 167		P02522	2bb2	
Met J. 16.5	147	16 452		Q57733	1shs	
Wheat 16.9	151	16 722		S21600[c]	1gme	
Spherulin 3a	103	11 285		P09353	1ha4	
Protein S	173	18 793		P02966	1nps[d]	
Enzyme-crystallins with X-ray structures						
δ-crystallin	466[e]	51 043[e]		P05083[e]	1ioa	
η-crystallin	501	54 537		Q28399	1o9j	

[a] Structure of C-terminal domain.
[b] Sequence printed in Norledge et al. (1997a).
[c] The sequence is from GenBank with one sequence change T7S.
[d] Structure of the N-terminal domain.
[e] The sequence is from chicken, the 3D structure is of the turkey protein.

2.3 The α-crystallins

2.3.1 Primary, secondary and tertiary structure

There are two α−crystallin genes, αA and αB, encoding proteins that share around 60% sequence identity (Bloemendal and de Jong, 1991). αA−crystallin is the lens-specific member of the family. In fact, only traces of it are found in some other tissues (Srinivasan, 1992). On the other hand, αB−crystallin is more widely expressed, and particularly abundant in brain, heart and muscle (Iwaki, 1990). In man, the ratio of αA- to αB-crystallin in the foetal lens is about 2:1 and the ratio decreases to about 3:2 in the water-soluble fraction of a lens from a 54/55 year old (Ma, 1998). The α-crystallins are presumed to function both as structural proteins and as chaperones in the lens (see section 2.3.3)

CD- and IR-based secondary structure predictions for the α-crystallin subunit suggested predominantly β-sheet and less than 20% helix content. Due to the polydisperse size distribution of both the natural and recombinant protein, crystallization of vertebrate α−crystallin has been unsuccessful so far. Thus, neither the detailed 3D structure of the subunit nor the topology of the subunit assembly is presently known. It is only known from their primary structure that both α-crystallins contain a particular amino-acid sequence called the ''α-crystallin domain'' shared by all the members of the sHsps (de Jong, 1998): sHsp sequences are characterized by a C-terminal ''α−crystallin domain'' linked to a variable N-terminal region (de Jong, 1998). It was proposed that the ''α−crystallin domain'' might resemble an Ig fold (Mornon, 1998). This hypothesis was confirmed when the 2.7 Å X-ray structure of an ''α−crystallin domain'' was solved from an the first sHsp assembly from a higher organism, wheat (van Montfort, 2001).
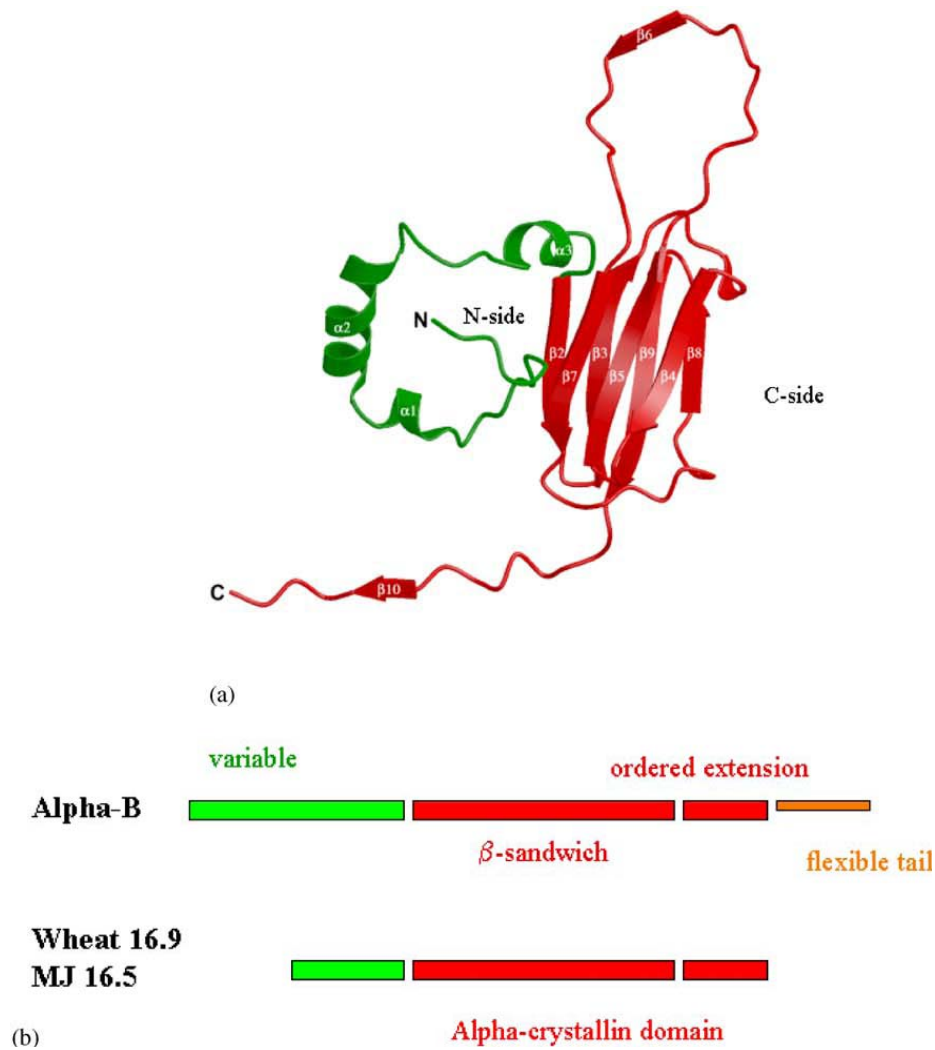
FIGURE 2. Structure of a wheat small heat shock protein (based on Fig. 2 from van Montfort et al., 2001). (a) Ribbon diagram of the protein with the N-terminal arm shown in green, the α-crystallin domain and C-terminal extension in red with the N- and C-termini, and secondary structure elements labelled. (b) The conserved α-crystallin domain as recognized by sequence profile searches is shown in red. It comprises two structural modules, the β-sandwich and the ordered extension. The hinge connecting these two modules is flexible allowing different assemblies. The flexible tail is shown in orange and corresponds to the regions classed as mobile when the assembly is investigated by NMR spectroscopy. The N-terminal regions (green) are variable in length and sequence.

Looking in detail at one monomer of this sHsp (Fig. 2a), the domain fold is seen to be composed of a two sheet β−sandwich structure surrounded by ''loose ends'', in contrast with the neat arrangement of strands in the βγ−crystallin domain (see section 2.4). This is considered to represent an ''unfinished domain'', as the edges of both sheets on the two sides of the sandwich (labelled the N- and C-sides) need partners for stabilization of the fold. The ''α−crystallin

domain'' in the α−crystallins is likely to have the β−sandwich fold in which the C-side protection is provided by an ordered extension of a partner subunit. The α−crystallins also have an additional C-terminal tail for which there is evidence of conformational flexibility (Fig. 2b).

2.3.2 Quaternary Structure

Vertebrate α-crystallins, like many sHsps, form polydisperse multimers (MacRae, 2000). α−Crystallins have molecular masses between 300 and 1200 kDa, depending on the solvent conditions and other variables. These multimers contain about 40 subunits of αA− and αB−crystallin in a ratio of 3 to 1 (for review, see Horwitz, 2003). α−Crystallin can be readily denatured by heat and Ca^{2+}, following pathways that include both changes in the secondary structure and the state of assembly (Doss-Pepe, 1998; Putilina, 2003).

To monitor the heat-induced changes that occur in the structural domain of lens α-crystallin diverse techniques like circular dichroism, fluorescence, differential scanning calorimetry, were used (Tardieu, 1986; Walsh, 1991). Based on these results a model is proposed by Tardieu (Tardieu, 1986) and extended by Walsh (Walsh, 1991). The proposed model of native α-crystallin has a three-layer structure in which the inner layer (core) is a micelle containing 12 subunits arranged as a cuboctahedral symmetry (fig. 3a). The apolar region is directed inward constituting a hydrophobic core similar to a micelle and adding structural stability. A second layer of six subunits has similar but not identical structure to the first layer, directing its apolar face toward the hydrophobic core (fig. 3b). Thus, these two layers constitute a micelle-like structure with octahedral symmetry. The third layer adds more subunits for a total of not more than 42 (Fig.3c)**. T**he inner two-layer structure of molecular mass 360 kDa is highly stable called $α_M$. The three-layer structure of the native protein, instead, is rather unstable. At nearly 45 °C the outer layer dissociates from the inner two

layers, and at higher temperatures (45-60°C) rapidly reassociates to a slightly modified two-layer structure with a stability similar to that of α_M (Fig. 3d). The proposed model does not require any specific assembly of the αA and αB subunits in each layer, but the fluorescence results suggest that the native inner two layers probably contain mostly αA.
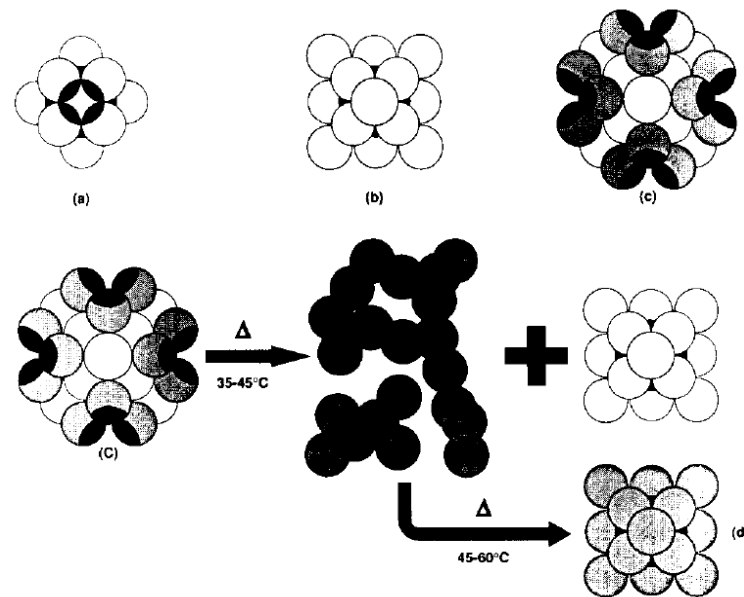

FIGURE 3.   Schematic representation of the proposed model. (a) the first, innermost layer consists of 12 subunits (b) first and second layers comprise a total of 18 subunits, arranged as a cuboctahedral symmetry. (c) first, second, and third layers comprise a total of 42 subunits, cuboctahedron type. The hydrophobic portion is shown in black. (d) a two-layer structure, similar but not identical to (b), formed upon heating the original three-layer structure (c).

Also Ca^{2+} alters the structural stability of α-crystallin leading to the formation of aggregates. Ca^{2+}-induced aggregation of lens α-crystallin was initially studied by sedimentation analysis (Jedziniak, 1972) and the possible role for Ca^{2+} in the cataractogenesis process was discussed (Jedziniak, 1983; Duncan, 1984). Indeed, In human lenses with dense, highly localised opacities, Ca^{2+} distribution is not uniform and is highest in regions that scatter most light (Duncan, 1977). Recently, it was found that γ−crystallin from bovine lenses shows significant calcium-binding ability (Rajini, 2001), the greek key $\beta\gamma$−crystallin fold (see section 2.4) being the calcium-binding motif. The effect of Ca^{2+} on the thermal stability of α−crystallin by UV and Fourier-transform infrared (FTIR) spectroscopies has been investigated (Del Valle, 2001). In both

cases, a Ca^{2+} -induced decrease in the midpoint of the thermal transition is detected. The presence of high $[Ca^{2+}]$ results also in a marked decrease of its chaperone activity in an insulin-aggregation assay. The results obtained from the spectroscopic analysis, and confirmed by circular dichroism (CD) measurements, indicate that Ca^{2+} decreases both secondary and tertiary–quaternary structure stability of α–crystallin. It is concluded that Ca^{2+} alters the structural stability of α-crystallin, resulting in impaired chaperone function and a lower protective ability towards other lens proteins, playing in that sense a role in the progressive loss of transparency of the eye lens in the cataractogenic process.

2.3.3 Lens α-crystallins and chaperone function

Like the α-crystallin, the other sHsps usually associate into high molecular weight monodisperse or polydisperse oligomers, able to protect against stress through the binding of a variety of partially unfolded substrates. α–Crystallin was demonstrated by Horwitz (Horwitz, 1992) to exhibit such chaperone properties in vitro. On the basis of these results, Horwitz proposed that α–crystallin would bind β–crystallin or γ–crystallin at the onset of their denaturation, thus preventing further precipitation and lens opacity.

The chaperone-like activity of α-crystallin depends on temperature (Raman and Rao, 1997). It is less pronounced below 30 °C and is enhanced above this temperature. The transition above at nearly 45 °C already investigated by Walsh, involving a quaternary structural transition and an enhanced or reorganized hydrophobic surfaces of α-crystallin, probably forms a part of the general mechanism of the chaperone function that is required more effectively in hypertermic and stressful conditions for the lens cell.

2.4   The β- and γ-crystallins

The β−crystallins are a family of basic (βB1, βB2, βB3) and acidic (βA1, βA2, βA3 and βA4) polypeptides (Herbrink et al., 1975; Berbers et al., 1984). The sequences of their corresponding globular domains exhibit between 45 and 60% identity with each other, and about 30% with γ−crystallins.

The oligomeric β− and the monomeric γ−crystallins are both built up out of four "Greek key" motifs organized into two domains. This common secondary structural motif has the typical shape of Attic vases (Fig. 4a).
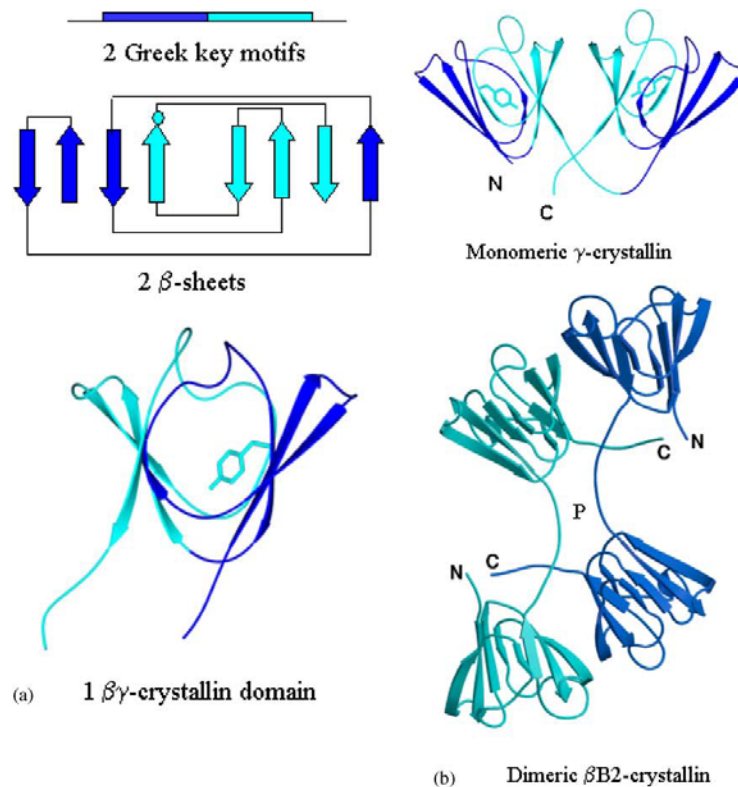

FIGURE 4.   The modular structure of the βγ-crystallins. (a) Each βγ-crystallin domain is made from two linear sequence related Greek key motifs that intercalate on folding to form two β-sheets. The second motif (shown in turquoise) is more sequence conserved among family members and contains a tyrosine corner positioned between the 3rd and 4th β−strands (indicated by the turquoise filled circle). The two sheets form a compact and pseudo-symmetric βγ-crystallin domain. (b) All lens βγ-crystallins comprise two domains. In the monomeric γ-crystallins the N-and C-terminal domains pair in a symmetrical manner about an approximate dyad using mainly residues from motifs 2 and 4. In the dimeric βB2-crystallin, the N-terminal domain pairs with the C-terminal domain of the partner subunit, in a process known as domain swapping.

The two consecutive Greek key motifs comprising eight β–strands intercalate to form two β–sheets that pack together to form a β–sandwich domain.

Although β–sandwich domains are common in proteins, in βγ–crystallins they are characterized by an high internal conformational symmetry and by a conserved folded hairpin structure for each motif. Sequence–structure alignment of all the Greek key motifs shows that two quite distal residues, a glycine and a serine, are the most conserved and are involved in stabilizing the supersecondary fold by packing this β–hairpin over the β–sheet (Blundell et al., 1981).
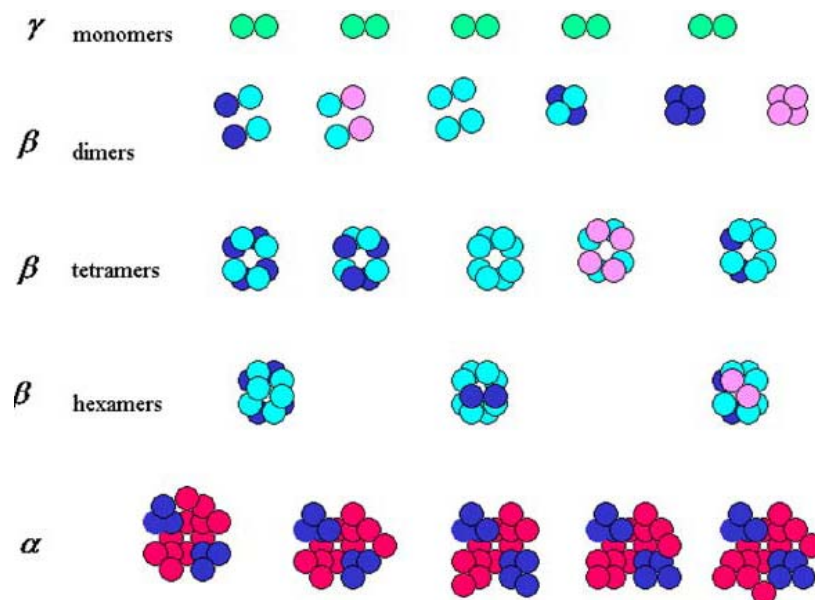

FIGURE 5.   Structural polydispersity in the lens crystallins. The lens αβγ-crystallins constitute an array of differently sized proteins. Although the γ-crystallin family members are individually monodisperse, the oligomeric crystallins have the potential of greater polydispersity. In the case of dimeric β-crystallins, not only is there a potential combinatorial diversity due to the identity of monomer components, but also the possibility of conformational diversity generated through use of interface selection in subunit pairing. This diversity can then only be increased in the higher order β-crystallin assemblies, although little precise information is available about them. In the case of α-crystallin, not only is there the potential for diversity in the location of the αA- and αB-crystallin subunits in the assembly, there is also evidence for variation in the number of assembly subunits. The α-crystallin cartoon is based on the model of heteromeric lens α-crystallin by Tardieu and colleagues (Tardieu et al., 1986).

The main sequence difference between monomeric γ-crystallins and oligomeric β-crystallins is the presence of sequence extensions in the oligomers which permits the linkage between monomers (Fig. 4b). The βγ−crystallin domain system is thus certainly versatile in terms of domain assembly and may well have evolved to generate conformational and combinatorial diversity in the oligomeric β−crystallins. Not only might this be a device for inhibiting crystallization at the high protein concentration of the lens, but it could also contribute to forming a range of oligomeric sizes. In turn these contribute to an even protein distribution and refractive index (Fig. 5). Although higher assemblies of β−crystallins can be made *in vitro*, the size reached is not yet as large as the *in vivo* assemblies.

3. Modeling nucleation-aggregation kinetics

3.1 Colloidal systems and protein systems

Colloidal science has advanced to a great extent over the last forty years being inspired by and inspiring applications. The large variety of colloidal systems that can be prepared or found in nature provide rich possibilities to gain insight into phenomena and processes of interest to physicists, chemists, biologists, material and environmental scientists, and engineers. This explains the broad spectrum of papers published on the various aspects of colloidal science.

The kinetics of aggregation has been a topic of scientific efforts since the pioneering work of Marian von Smoluchowsky at the beginning of the previous century (von Smoluchowky, 1917). He derived the first aggregation rate constants for systems where only Brownian forces cause the motion of the particles and the collisions between them. He considered the case where the particles are completely destabilized and their interactions are dominated only by attractive forces, resulting in the formation of a new cluster upon any

collision between two particles. This constitutes the fastest aggregation rate possible. The aggregation kinetics of particles that are not fully destabilized but retain some repulsive forces in addition to the attractive ones, has been described by Fuchs almost 20 years later (Fuchs, 1934). He introduced the concept of a relative aggregation rate, given as the ratio of the fastest aggregation rate derived by Smoluchowsky to the one observed in only partially destabilized systems. This important parameter for colloidal science is called the *Fuchs* stability ratio. Later the Derjaguin-Landau-Verwey-Oveerbek theory (DLVO) has been overly successful in providing a qualitative and to some extent even quantitative framework to calculate the stability ratio (Verwey, 1948; Derjaguin, 1989; Bostrom, 2001). Their work breeded the concept of population balance equations which has been used in many applications in order to model distributed particulate populations and the changes they undergo as a function of time or other system variables (Ramkrishna, 2000). The population balance equations (PBE) for aggregation form the basis of the investigations presented in this thesis.

Besides the colloidal stability, the structure of aggregates evolving in colloidal dispersions of small particles has long puzzled scientists due to its seemingly complex nature. Mandelbrot, with his breakthrough concept of fractal geometry (Mandelbrot, 1982), sparked renewed interest in colloidal aggregation by providing a framework which allowed to characterize the random structure of an aggregate in an average way by a simple power-law relation between its mass and radius, $i \sim R^{d_f}$, where i is the number of particles in a cluster and R its radius (Forrest, 1979; Witten, 1981).

The exponent d_f, the fractal dimension, can be used to describe how open or dense a certain aggregate is. This exponents takes values smaller than three and therefore fractal aggregates are characterized by a density decreasing with increasing number of particles in the cluster.

Later, in a series of hallmark papers, Lin et al. (Lin, 1989; Lin, 1990) have shown by using dynamic and static light scattering that colloidal aggregation exhibits two universal limits: these are diffusion limited colloid aggregation (DLCA), characterized by a complete destabilization of the colloidal particles with aggregation taking place upon every collision, and reaction limited colloid aggregation (RLCA), where some remaining repulsive electrostatic forces allow only a small fraction of collisions to result in the formation of a new aggregate. The structure of the aggregates in DLCA is rather open and fractal dimensions of $d_f \sim 1.8$ have been found both in experiments and computer simulations (Odriozola, 1999). Depending on which aggregation model is used to simulate DLCA, two kind of shapes of the cluster mass distribution (CMD) are predicted. When using a constant aggregation kernel, the predicted CMD is rather flat (Lin, 1990). However, when properly accounting for the size dependence of the aggregation rate constant, the predicted CMD exhibits a bell shape, which differs from the previous one in the smaller aggregate size region (Odriozola, 1999). Both these CMDs in DLCA have a sharp cut-off at a certain mass, which itself grows with a power law behaviour in time (Lin, 1990).

The lower sticking probability in RLCA results in denser aggregates with $d_f \sim$ 2.1, which was also confirmed in experiments and computer simulations (Lin, 1990). The CMD in RLCA is characterized by a power law shape with an exponent τ_c = 1.5 and a sharp cut-off. Here, the cut-off mass grows exponentially in time (Lin, 1990). Importantly, Lin et al. demonstrated that these regimes exist for different colloidal systems (gold, silica and polystyrene).

Since then, the aggregation kinetics of several different colloidal particle systems has been studied in dilute conditions. Among these systems, charge stabilized polystyrene latexes in aqueous solution play an important role as model systems. In particular, the stability behaviour of polystyrene spheres with different charged functional groups as a function of electrolyte concentration, pH and the amount of additional charged and/or steric surfactant has been

analyzed in detail (Behrens, 2000; Peula, 1998, Sefcik, 2003; Romero-Cano, 1998, Porcel, 2001).

Also biological systems like globular proteins or milk are often analyzed in the framework of aggregation discussed above (Weijers, 2002; Durand, 2002). The aggregation behaviour observed in all of these systems is often compared to the classification given by the limiting regimes, i.e. DLCA and RLCA. The supramolecular aggregation of α-crystallin, induced by generating heat-modified α-crystallin forms and by stabilizing the clusters with calcium ions, was investigated by means of static and dynamic light scattering by our group (Andreasi Bassi et. Al, 1995). The kinetic pattern of the aggregation and the structural features of the clusters can be described according to the RLCA model previously adopted for the study of colloidal particles aggregation systems. The structure factor of the clusters is typical of fractal aggregates. A fractal dimension d_f =2.05 was determined, indicating a low probability of sticking together of the primitive aggregating particles.

The conclusion of the foregoing discussion is that various aggregation mechanisms and cluster structures have been observed in a variety of colloidal and biological systems. However, the application of colloidal aggregations theories to proteins systems is often insufficient because it lacks the modelization of diverse protein related phenomena, like nucleation and unfolding. The importance of knowing unfolding, nucleation and aggregation rates in protein folding diseases requires a detailed model accounting for the unfolding process and the nucleation process.

Furthermore, a systematic comparison of the corresponding CMD obtained by solving the PBE, with an appropriate experimental characterization of the CMD, is still missing. This experimental characterization of aggregation in the sub-micron size range relies primarily on static and dynamic light scattering techniques (Lin, 1990; Sorensen, 2001), which consequently requires a detailed model for light scattering to calculate these quantities from the PBE.

The cluster mass distribution (CMD) and the aggregate size distribution, which obviously depend crucially on the processing conditions, in fact completely characterize the aggregation process.

3.2 Aggregation kinetics in colloidal systems

3.2.1 Population balance equation

Population balances (PBE) are general conservation laws applicable to a variety of particulate systems (Ramkrishna, 2000). Aggregation in homogeneously mixed colloidal dispersions can conveniently be described by PBE, where we use mass as the internal coordinate for representing aggregates undergoing birth and death events. These events lead to the formation and disappearance of aggregates of mass m and indicating with n_i (t) the number of aggregates of mass $m = i \, m_0$ at time t we obtain the following form of the population balance:

$$\dot{n}_i(t) = \frac{1}{2}\sum_{j=1}^{s} K_{i-j,j} \; n_{i-j}(t)n_j(t) - n_i(t)\sum_{j=1}^{\infty} K_{i,j} \; n_j(t) \qquad (3.1)$$

where the two terms on the right-hand side represent the rate of birth and death of units of mass $m = i \, m_0$ per unit volume, respectively. The first one represents the production of aggregates of mass $m = i \, m_0$ by aggregation of two smaller aggregates of mass m' and $m - m'$, while the second considers the loss of particles of mass m due to aggregation with any other aggregate of mass m'. The aggregation frequency function $K_{i,j}$ accounts for two physical factors, which constitute the aggregation process: the collision frequency between two particles and the corresponding sticking efficiency.

The validity of the PBE in the form of equation (3.1) relies on several assumptions. In particular, in concentrated systems it can be expected that more than two particles undergo aggregation simultaneously and that the presence of surrounding particles influences the two aggregating ones. On the other hand, in

equation (3.1) only binary aggregation events are considered. The pair probability function $p_2(m,m',t)$ which accounts for the probability of finding two particles of mass *m* and *m'* undergoing aggregation at the same spatial location in the time interval fit, is computed by assuming an independent probability of finding each of the two involved aggregates in the system, i.e. $p_2(m,m',t) = p_1(m,t)p_1(m',t)$. This assumption is known as the closure hypothesis and has been discussed in the literature (Ramkrishna, 1976).

At the other extreme of diluted systems, where the population is constituted by only a few particles, it has been shown that the PBE (3.1) fails and single statistical events become important (Sampson, 1985). This is due to the fact that in diluted systems the few particles present are correlated, meaning that the relation $p_2(m,m',t) = p_1(m,t)f_1(m',t)$ fails and higher order product density functions $p_2(m,m',t), p_3(m,m',m'',t),....., p_M(m,m',m'',....,m^M,t)$ have to be used in addition to the first-order functions used in equation (3.1).

No attempt is made in the following to *a priori* determine the upper and lower concentration bounds, where the aggregation PBE in the form of equation (3.1) is accurate. This would not be a straightforward task and therefore we ultimately rely on the comparison with experimental data.

3.2.2 Numerical solution and reconstruction of the CMD

The description of aggregation phenomena in the framework of population balances requires the coverage of several order of magnitudes in aggregate size. Primary particles in colloidal dispersions usually are in the size range of 5 - 500nm. Aggregation of these particles frequently results in clusters up to the size of 300 μm. Under certain operating conditions the formation of coagulum can occur, the radius of which can attain values up to 1 - 100mm.

Accordingly, in order to describe the evolution of the CMD over the whole range of particle and aggregate sizes, a simple linear discretization technique would result in a number of coupled ODE's not solvable in reasonable computer time. Thus, the application of a geometric or other expanding grids for the representation of particle sizes is indispensable for computational efficiency. A widely used method of approximation is the Runge-Kutta method (Forsythe, 1977). It uses a sampling of slopes through an interval and takes a weighted average to determine the right end point.

We implemented a homemade software with Labview 7.1, that uses this method to solve PBE systems of non-linear differential equations.
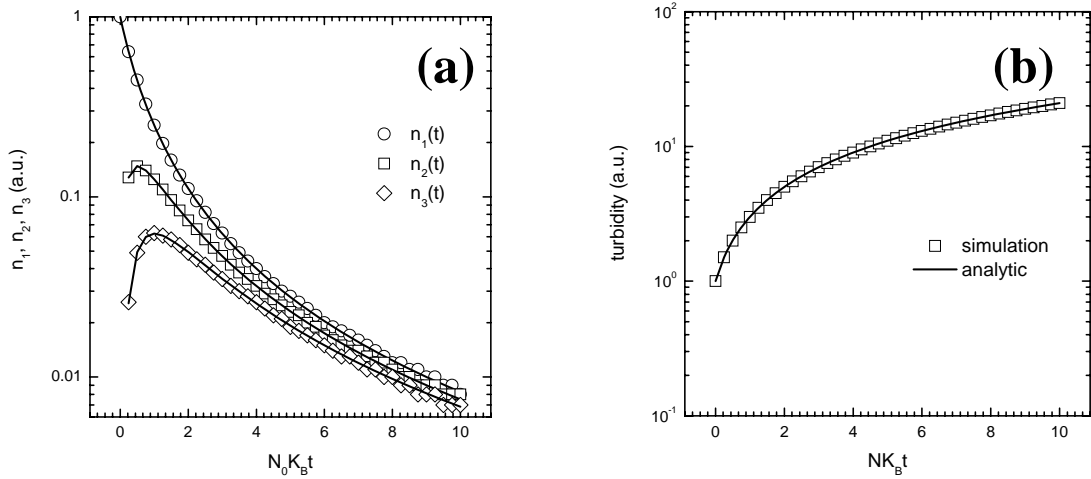

FIGURE 6. Comparison between the analytical (Eq. 2.2) and the numerical RK solution for equation(3.1) with the constant kernel $K_{i, j} = K_B$. (a) Discretized analytical solution for $n_1(t)$, $n_2(t)$ and $n_3(t)$ (solid line) and KR numerical solution; (b) continuous analytical solution for $\tau = \sum_i i^2 n_i$ (solid line). and reconstructed numerical KR solution.

One important oft-neglected aspect is the reconstruction of the continuous distribution from the discretized one obtained from the *RK* method. To illustrate this point we consider the PBE (3.1) with a constant aggregation kernel, i.e. $K_{i,j} = K_B$, for which an analytical solution exists:

$$n_i(t) = n_0 (K_B n_0 t)^{i-1} (1 + K_B n_0 t)^{-i-1} \qquad (3.2)$$

29

where n_i denotes the number of clusters of a certain dimensionless mass $i =$ m_i/m_1, where m_i is the mass of a cluster with i primary particles and m_1 is the primary particle mass. In Figure 6(a) the discretized solution for $n_1(t)$, $n_2(t)$ and $n_3(t)$ obtained with the *RK* method is compared with the corresponding values obtained using the analytical solution (3.2). It is seen that the obtained values are in satisfactory agreement, thus indicating that the numerical *RK* method provides reliable results. The next point is to compare a function of all the $n_i(t)$'s, for example an experimentally accessible quantity like turbidity $\tau = \sum_i i^2 n_i$ obtained with the *RK* method with the corresponding values obtained using the analytical solution (3.2). The obtained results are compared in Figure 6(b) and again the agreement is satisfactory, thus indicating that, although very simple, this reconstruction procedure provides reliable results.

Another relevant point in computing CMDs numerically is that the size range for the problem on hand has to be specified "a priori" by an upper and a lower bound, here conveniently denoted in terms of aggregate mass m_0 and m_M, where *M* denotes the number of pivots in the discretized interval of aggregate mass. It should be noted that if the aggregates grow to such an extent that they reach the upper bound, and this is allowed to undergo further aggregation, the generated aggregates would be lost since they would exit the discretized size range and consequently the mass of the dispersed phase would not be conserved. To avoid this, we have to close the boundary by a collective pivot (i.e. the largest size m_M), which includes all aggregates larger than m_M and is excluded from the aggregation process. By properly applying this closure procedure, it is possible to satisfy the mass balance, which is particularly useful when dealing with systems that can produce aggregates of very large size, as in the case of polymer or colloidal gelation (Krall, 1998; Butte, 2002). However, this situation does not occur in any of the computations shown in this work and the last pivot always contains a negligible mass.

3.2.3 Characteristics of aggregate populations

In many applications one is interested in the size of the aggregates, expressed in terms of volume or radius. Since the PBE discussed above provides a cluster mass distribution (CMD), the question arises of how the mass of an aggregate can be related to its size. In the case of coalescing particles this is straightforward since the spherical shape is conserved upon aggregation. In the case of aggregates constituted of primary particles rigidly adhering at their surface contacting points, we obtain randomly shaped aggregates that are usually described through the fractal scaling relation (Sorensen, 2001):

$$ i = \frac{m_i}{m_1} = k_f \left(\frac{R_{g,i}}{R_p} \right)^{d_f} \qquad (3.3) $$

where d_f is the fractal dimension, m_1 and R_p denote the mass and radius of a primary particle, while m_i and $R_{g,\,i}$ those of an aggregate. The prefactor k_f is a constant of the order of unity (Sorensen, 1997). The radius of gyration $R_{g,\,i}$ in equation (3.3) is connected to the hydrodynamic radius $R_{h,\,i}$ by a factor β_i, typically of the order of one depending on the fractal dimension d_f (Lin, 1990, Wiltzius, 1987).

$$ \beta_i = \frac{R_{h,i}}{R_{g,i}} \qquad (3.4) $$

Having set a fractal dimension value, equations (3.3) and (3.4) provide the average aggregate radii $R_{g,\,i}$ and $R_{h,\,i}$ as a function of the corresponding mass m_i. In selecting a quantity to define the size of an aggregate it is convenient to adhere to quantities that can be measured experimentally. Accessible non-integer moments of CMD are the radius of gyration $< R_g^2 >$ when using static light scattering (SLS), and the mean hydrodynamic radius $< R_{h,eff} >$, when using dynamic light scattering (DLS). In order to compare these experimental values with the cluster mass distribution n_i, obtained from equation (3.1), we need to relate the averages $< R_g^2 >$ and $< R_{h,eff} >$ of the entire cluster mass distribution to

the corresponding radii of the individual aggregates of mass i, given by $R_{g,\,i}$ and $R_{h,\,i}$. In the case of the radius of gyration, which relates to the mass distribution inside the aggregate, such a relation is simply given by (Pusey, 1987)

$$< R_g^2 >= \frac{\sum_i i^2 n_i R_{g,i}^2}{\sum_i i^2 n_i} \qquad (3.5)$$

In the case of the hydrodynamic radius, which actually reflects the diffusion of the aggregate, the corresponding relation is more complex since it has to account for the effect of the measurement angle, the aggregate structure and the complex diffusion processes of the aggregates (Lin, 1990; Pusey, 1987):

$$< R_{h,eff} >= \frac{\sum_i i^2 n_i S_i(q)}{\sum_i i^2 n_i S_i(q) R_{h,i}^{-1}} \qquad (3.6)$$

where $S_i(q)$ represents the structure factor of the aggregates of mass i and $R_{h;i}$ his hydrodynamic radius. A third average of interest in this thesis is the average scattered intensity, measured by static light scattering, which is obtained by intensity weighted averaging of the individual cluster structure factors $S_i(q)$ by

$$I(q) = K \sum_i i^2 n_i S_i(q) \qquad (3.7)$$

Where K is a constant accounting for instrument specificities and for the $\partial n / \partial c$ of the suspension. Among the various possibilities for computing the structure factors of individual aggregates (Sorensen, 1999) we have chosen the Fisher-Burford relation not only for its simplicity but also because it has been shown to be quite accurate for aggregates having fractal dimensions equal to about 2 (Sorensen, 2001). This is given by

$$S_i(q) = \left(1 + \frac{2}{3d_f} (qR_{g,i})^2 \right)^{-\frac{d_f}{2}} \qquad (3.8)$$

where q denotes the scattering wave vector, given by the relation:

$$q = \frac{4\pi n}{\lambda_0} sen\left(\frac{\vartheta}{2}\right) \qquad (3.9)$$

Where n is the refractive index of the liquid medium, λ_0 the wavelength of the used light and θ the scattering angle.

The Kirkwood–Riseman theory has been used to derive an analytical formula for the evaluation of $R_{g,\,i}$ and $R_{h,\,i}$ of fractal clusters. The proposed relation is based on knowledge of the particle–particle correlation function and can be applied to clusters containing any number of particles larger than 4. Consequently, we have used the following relation, recently derived using Monte Carlo simulations (by means of an off-lattice cluster– cluster aggregation algorithm) and valid for aggregates containing more than four particles (Tirado Miranda, 2003; Lattuada, 2003),

$$g(r) = \begin{cases} 0 & \text{for } r < 2R_p \\[2mm] \dfrac{N_{nn}}{4\pi(2R_p)^2}\,\delta(r - 2R_p) & \text{for } r = 2R_p \\[2mm] \dfrac{a}{R_p^{b+3}}\,r^b & \text{for } 2R_p < r < 4R_p \\[2mm] \dfrac{c}{R_p^{d_f}}\,r^{d_f-3}\exp\!\left(-\left(\dfrac{r}{\xi}\right)^{\gamma}\right) & \text{for } r > 4R_p \end{cases} \qquad (3.10)$$

where N_{nn} is the average number of nearest neighbour particles, $\delta(x)$ is the Dirac delta function, and a and b are two parameters describing the structure of the second coordination shell, while c, d_f, ξ, and γ represent an empirical constant factor, the fractal dimension, the cut-off length, and the cut-off exponent, respectively. While the fractal dimension d_f is the same for all DLCA (equal to 1.85) and RLCA clusters (equal to 2.05), all the other parameters change as the number of particles in the clusters changes. For the cut-off length the following fractal scaling has been adopted,

$$\xi = \alpha R_p i^{\frac{1}{d_f}} \qquad (3.11)$$

where the constant α equals 1.45 and 1.55 for DLCA and RLCA clusters, respectively. The behaviour of the parameters a, b, N_{nn}, and γ as a function of the number of particles in the cluster i is described by the same equation,

$$F(i) = d\frac{(i-e)^n}{(i-e)^n + f} \qquad (3.12)$$

where the empirical parameters d, e, and f take different values for the different parameters, as summarized in Table 2. These values have been obtained from the simulations performed by Tirado Miranda (Tirado Miranda, 2003). The value of the constant factor c is

$$c = \frac{i - 1 - N_{nn} - \frac{4\pi a}{b+3}\left(4^{b+3} - 2^{b+3}\right)}{\frac{4\pi}{\gamma}\left(\frac{\xi}{R_p}\right)^{d_f}\Gamma\left(\frac{d_f}{\gamma}\right)\left(1 - \Gamma_{inc}\left(\left(\frac{4R_p}{\xi}\right)^{\gamma}, \frac{d_f}{\gamma}\right)\right)} \qquad (3.13)$$

table 2

Values of the parameters d, e, f, and m in Eq. (17) to compute the parameters of the particle–particle correlation function (15): N_{nn}, a, b, and γ as functions of the number of particles per cluster for both DLCA and RLCA

Parameters of the $g(r)$ function	Aggregation mechanism	d	e	f	m
N_{nn}	DLCA	2.0342	1.1477	0.9997	1
	RLCA	2.0415	1.1511	1.0086	1
a	DLCA	0.0095	4.1292	0.1997	2
	RLCA	0.0138	2.7544	4.1792	2
b[a]	DLCA	0.6425	6.2352	5.1747	1
	RLCA	0.4857	9.6836	11.6665	1
γ	DLCA	2.1976	3.8377	−0.1784	1
	RLCA	2.16	0.1966	−3.5926	2

[a] The value of the b parameter is zero for DLCA clusters with $i < 7$ and for RLCA clusters with $i < 10$.

The advantage of the developed piecewise expression for $g(r)$ is that it describes quantitatively the behaviour of the first two coordination shells and of the fractal part. By substituting eq. (3.10) into the expression of the hydrodynamic radius of an aggregate $R_{h,i} = \dfrac{iR_p}{1 + R_p\int_0^\infty g(r)4\pi r dr}$ (Lattuada, 2003), the following expression for $R_{h,\,i}$ is obtained,

$$R_{h,i} = iR_p \left[1 + \frac{N_{nn}}{2} + \frac{4\pi a}{b+2} \left(4^{b+2} - 2^{b+2} \right) + \frac{4\pi c}{\gamma} \left(\frac{\xi}{R_p} \right)^{d_f-1} \Gamma \left(\frac{d_f-1}{\gamma} \right) \left(1 - \Gamma_{inc} \left(\left(\frac{4R_p}{\xi} \right)^{\gamma}, \frac{d_f-1}{\gamma} \right) \right) \right]^{-1}$$

(3.14)

where Γ and Γ_{inc} are the Euler gamma function and incomplete gamma function, respectively (Zhu, 1994). This formula makes it possible to calculate the value of the hydrodynamic radius of a fractal aggregate readily, once the parameters appearing in the correlation function are known.

The analytical formula for the evaluation of $R_{g,i}$ is (Tirado Miranda, 2003),

$$R_{g,i} = R_{g,p}^2 + \frac{R_p^2}{2i} \left(4N_{nn} + \frac{4\pi a}{b+5} \left(4^{b+5} - 2^{b+5} \right) \right) + \frac{4\pi c R_p^2}{2i\gamma} \left(\frac{\xi}{R_p} \right)^{d_f+2} \Gamma \left(\frac{d_f+2}{\gamma} \right) \left(1 - \Gamma_{inc} \left(\left(\frac{4R_p}{\xi} \right)^{\gamma}, \frac{d_f+2}{\gamma} \right) \right)$$

(3.15)

where $R_{g,p}$ is the primary particle radius of gyration (for a sphere $R_{g,p} = \sqrt{\frac{3}{5}} R_p$).

Substituting now in equations (3.5) and (3.6) and (3.7) the expressions of the gyration and hydrodynamic radii of the aggregates, $R_{g,i}$ and $R_{h,i}$, given by equations (3.14) and (3.15), we can compare the experimentally accessible quantities $I(q)$, $<R_g^2>$ and $<R_{h,eff}>$, with that computed from the cluster mass distribution n_i by solving the PBE (3.1). It is worth nothing that the gyration and hydrodynamic radii represent different non-integer moments of the CMD, and therefore provide information not only on the average value but also on the higher order moments of the CMD. Accordingly, comparison of calculated with experimental values of both $<R_g^2>$ and $<R_{h,eff}>$ is a challenging test for the reliability of an aggregation kinetic, and therefore provides the possibility of discriminating among different kinetic models with respect to various aggregation conditions. In order to compute $I(q)$, $<R_g^2>$ and $<R_{h,eff}>$ from the equations above we need to know the fractal dimension, d_f. This quantity is measurable from SLS (Lin, 1990), measuring the angular distribution of scattered intensity (See chapter 4, § 4.2.1)

3.2.4   Forms of the aggregation kernel

In this section we discuss kernel equations for diffusion limited (DLCA) and reaction limited (RLCA) cluster aggregation that have been presented earlier in the literature.

3.2.4.1   DLCA-kernel

In the diffusion limited aggregation regime every collision between aggregates or primary particles is successful. The first and basic aggregation kernel for DLCA, accounting for the diffusive mobility ($D_i + D_j$) and the collision cross section ($R_i + R_j$) of aggregates, has been derived by Smoluchowsky (von Smoluchowsky, 1917). The diffusion coefficient D can be related to the radius of an equivalent sphere by the Stokes-Einstein relation $D_1 = k_B T / (6\pi\eta R_p)$. Using these relations and neglecting the size dependence of the aggregation rate by assuming equal sized particles, one obtains the *constant* aggregation kernel:

$$K_B = \frac{8 k_B T}{3\eta} \qquad (3.16)$$

To incorporate aggregate structure using the fractal concept, the aggregate size is assumed to scale with its mass according to equation (3.3). An equivalent scaling is assumed for the diffusion coefficient (Jullien, 1992), given by $D_i / D_1 = i^{-\frac{1}{d_f}}$. From these relations we obtain

$$K_{ij} = K_B B_{ij} \qquad with$$

$$B_{ij} = \frac{1}{4}(i^{-\frac{1}{d_f}} + j^{-\frac{1}{d_f}})(i^{\frac{1}{d_f}} + j^{\frac{1}{d_f}}) \qquad (3.17)$$

where B_{ij} is the matrix representing the collision cross section and the mobility of the two colliding aggregates. This kernel has been found to properly describe experimental data in DLCA (Lin, 1990).

3.2.4.2   RLCA-kernel

In RLCA only a fraction of collisions is successful in forming a new aggregate, due to the incomplete screening of the repulsive forces between particles. Considering primary particles, the reduced sticking efficiency due to repulsive forces and hydrodynamic interactions can be expressed by the Fuchs stability ratio (Melis, 1999),

$$W = 2R_p \int_{2R_p}^{\infty} \frac{e^{\frac{V}{k_B T}}}{G(h)h^2} dh \qquad (3.18)$$

where *G(h)* accounts for squeezing of the fluid between two approaching primary particles, *h* is the center to center distance and *V* is the particle interaction potential. This expression of the stability ratio applies only for primary particles and not for aggregates, that are composed of many primary particles. It has in fact been verified experimentally that the reactivity of aggregates increases with their mass (Lin, 1990; Broide, 1990), and therefore an additional factor P_{ij} has to be considered, leading to the following general RLCA kernel:

$$K_{ij} = W^{-1} K_B B_{ij} P_{ij} \qquad (3.19)$$

Let us review in the following the various RLCA kernels reported in the literature and recast them in the form introduced above. Using theoretical scaling arguments Ball et al. (Ball, 1987) concluded that the efficiency of aggregation is determined by the larger of the two aggregating clusters through a power λ. This parameter accounts for the increased aggregation efficiency of larger clusters due to a larger number of contact possibilities on their surface and it has been shown to be in the range $\lambda \in [1, 1.1]$ The resulting kernel can be written in terms of P_{ij} in equation (3.19) as follows:

$$P_{ij} = k^{\lambda}$$
$$k = \max\{i, j\} \qquad (3.20)$$

Other authors (Family, 1985) used the product kernel, given by

$$P_{ij} = (ij)^{\lambda} \qquad (3.21)$$

to simulate the CMD by a Monte-Carlo technique in the RLCA regime. They compared the obtained results with those given by the dynamic scaling theory, where the CMD obtained by Monte-Carlo simulations is represented by a dynamic scaling form. Relating these results to the Smoluchowsky equation and using equation (3.21) they a found non-trivial behaviour. There it has been pointed out that the asymptotic expressions of the dynamic scaling theory might not provide the exponent λ sufficiently accurately. In RLCA experiments using silica (Axford, 1997), it has been found, that the value of λ can vary in the range [0, 36; 0, 495], depending upon the solution ionic strength. In a study using a stochastic simulation method (Thorn, 1994), which compare the results to dynamic scaling theory as well as to experimental data (Broide, 1990), several values of λ have been tested. The following kernel has been shown to reproduce correctly the general features of the mass cluster distribution,

$$K_{ij} = W^{-1} K_B B_{ij} (ij)^{\lambda} \qquad (3.22)$$

where W is the Fuchs stability ratio and λ **=** 0.4 (de Hoog, 2001).

3.3   Extension of the model to protein systems: nucleation

As we stated in § 4.1, application of colloidal aggregation theories to proteins systems is often insufficient because it lacks the modelization of diverse protein related phenomena, like nucleation and unfolding. On the other hand, Kinetic studies have shown that the aggregation of proteins involved in these diseases follows a nucleation mechanism. In the next paragraph we present a brief description of the nucleation processes, and in the following one we will

develop a model that can account for the nucleation step in protein growth kinetics.

3.3.1   The Classical Nucleation Theory (CNT)

Nucleation is the process which starts a first-order phase transformation. It's a process consisting of the formation of nuclei of the new phase in the bulk of another phase. It's an activated process, as the growing nucleus of the new phase must overcome a free-energy barrier. It is the nucleus at the top of this barrier that determines the nucleation rate, with the rate decreasing exponentially as the barrier height increases. This makes the timescale for nucleation much larger than the characteristic time scale of the microscopic dynamics of the system. The basic physics of nucleation is best illustrated with the help of the classical nucleation theory (CNT) (Debenedetti, 1996; Oxtoby 1998; Garcia Ruiz, 2003). In homogeneous nucleation, CNT expresses the rate per unit volume k_N as the product of an exponential factor and a pre-exponential factor A

$$k_N = A\exp(-\Delta G^* / k_b T) \qquad (3.23)$$

The exponential factor is $\exp(-\Delta G^* / k_b T)$ where ΔG^* is the free energy cost of creating the critical nucleus, the nucleus at the top of the barrier. The physical meaning of A will be discussed extensively in section 4.3.2.

CNT treats the nucleus as if it were a macroscopic phase. If we restrict ourselves to the nucleation of one fluid inside the bulk of another phase, then the nucleus is spherical and its free energy has just two terms: a bulk and a surface term. If the nucleus has a radius R then the bulk term is the free energy change involved in creating a sphere of radius R of the new phase. The surface term is the free-energy cost of the interface at the surface of this sphere. Thus the free energy is

$$\Delta G = -\frac{4\pi}{3} R^3 \rho_n \Delta\mu + 4\pi R^2 \gamma \qquad (3.24)$$

where $\Delta\mu$ is the difference between the chemical potential of the phase where the nucleus is forming, and the chemical potential of the phase nucleating, γ is the interfacial tension, ρ_n is the number density of the nucleating phases. For nucleation from a dilute solution or suspension, the solution can be treated as an ideal gas and then $\Delta\mu/k_B T = \ln(\rho_b/\rho_{co}) = s$ where ρ_b and ρ_{co} are the number densities in the bulk phase in which nucleation is occurring, and at coexistence, respectively. The free energy at the top of the barrier, ΔG^*, is easily found by setting the derivative of ΔF to zero. Then we have

$$\Delta G^* = \frac{16\pi}{3} \frac{\gamma^3}{(\rho_n \Delta\mu)^2} \qquad (3.25)$$

This occurs for a critical nucleus of radius

$$R^* = \frac{2\gamma}{(\rho_n \Delta\mu)} \qquad (3.26)$$

Knowing ΔG^* and R^* is therefore possible to determine γ and $\rho_n \Delta\mu$.

3.4 Nucleation-Aggregation kinetics

3.4.1 Modeling the effect of nucleation

Kinetic studies have shown that the aggregation of proteins involved in protein folding diseases follows a nucleation mechanism, which resembles a crystallization process (see Figure 7). The critical event is the formation of protein oligomers that act as a nucleus to direct further growth of aggregates. Nucleation-dependent aggregation is characterized by a slow lag phase in which a series of unfavourable interactions forms an oligomeric nucleus, which then rapidly grows to form larger aggregates.
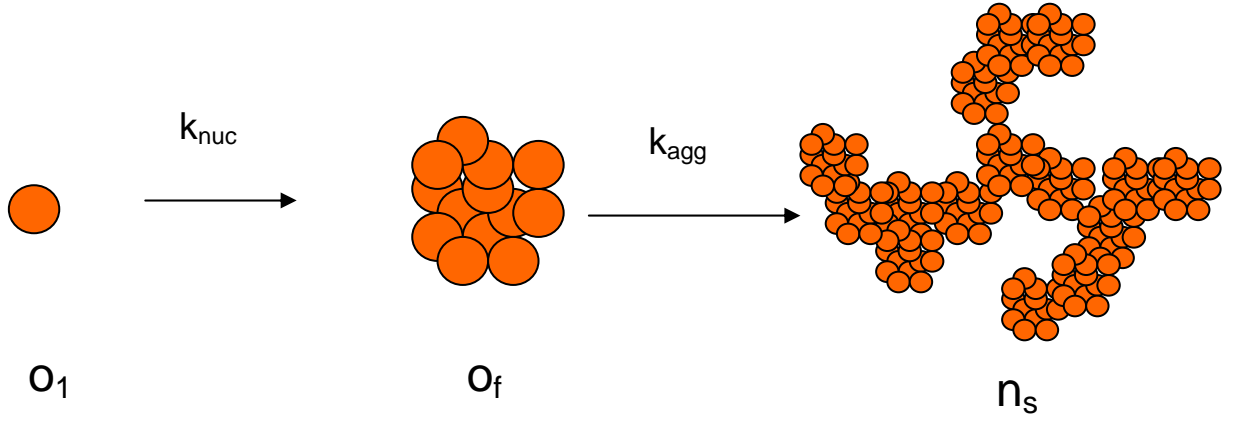
FIGURE 7   Schematic representation of the nucleation-aggregation process. The monomers o_1 form protein oligomers o_f that act as a nucleus to direct the further growth of aggregates n_s.

The aim of this section is to define a rigorous mathematical model that incorporates the physical chemistry of nucleation and the stochastic kinetics of aggregation and growth dynamics. A two-stage mechanism consisting of nucleation and stochastic aggregation is proposed.

The mechanism of nucleation is based on the Becker-Doring nucleation model from the field of atmospheric science (Seinfeld, 1998). Accordingly (figure 7), the monomers o_1, having mass m_0, react with one another as well as with different size oligomers so as to become larger clusters. The reactions between larger oligomers are negligible because their early concentrations and diffusivities are relatively low and small, respectively, as compared with the monomers. As oligomers grow, their chemical potentials drop, yet the surface tension to form new phases rises. Hence, there should exist a condition with minimum Gibbs free energy corresponding to the size of a cluster o_f (or nucleus), $M_C = N_c m_0$ (31). Any aggregates larger than the cluster would convert into the basic unit of the aggregation. Therefore, indicating with $o_s(t)$ the number of the growing oligomer of mass $m = s\, m_0$ at time t and indicating with $n_p(t)$ the number of the aggregates of mass $m = p\, M_C = p\, N_C m_0$ at time t, we obtain the following form of the population balance equations

$$\dot{o}_s(t) = K_{s-1,1}^N o_{s-1}(t) o_1(t) - o_s(t) K_{s,1}^N o_1(t) - \delta(s-1) o_1(t) \sum_{j=2}^{N_C-1} K_{j,1}^N o_j(t) \quad s = 1,....., N_C - 1$$

$$\dot{n}_p(t) = \frac{1}{2} \sum_{j=1}^p K_{p-j,j}^A \, n_{p-j}(t) n_j(t) - n_p(t) \sum_{j=1}^\infty K_{p,j}^A \, n_j(t) \qquad\qquad (3.27)$$

$$+ \delta(p-1) K_{N_C-j,j}^N o_{N_C-1}(t) o_1(t) \qquad\qquad p = 1,......, N_{agg}$$

where the two terms in the first equation on the right-hand side represent the rate of birth and death per unit volume of units of the nucleating oligomers, of mass $m = s \, m_0$, respectively. The nucleation frequency function $K_{i,j}^N$ accounts for two physical factors which constitute the nucleation process: the collision frequency between two particles and the corresponding sticking efficiency. The two terms in the second equation on the right-hand side represent the rate of birth and death per unit volume of the aggregating clusters, of mass $m = p \, M_C = p \, N_C \, m_0$, respectively. The aggregation frequency function $K_{i,j}^A$ accounts for the same physical factors proper of the nucleation process. The third term represents all the oligomers larger than the critical nucleus that are converting into the basic unit of the aggregation.

In the nucleation-aggregation model the averages $< R_g^2 >$, $< R_{h,eff} >$ and $I(q)$ of the cluster mass distribution become

$$< R_g^2 > = \frac{\sum_s s^2 o_s \left(R_{g,s}' \right)^2}{\sum_s s^2 o_s} + \frac{\sum_p p^2 n_p R_{g,p}^2}{\sum_p p^2 n_p} \qquad\qquad (3.28)$$

where $R_{g,s}'$ and $R_{g,p}$ are the corresponding gyration radii of the oligomers of mass s and aggregates of mass p,

$$< R_{h,eff} > = \frac{\sum_s s^2 o_s}{\sum_s s^2 o_s \left(R_{h,s}' \right)^{-1}} + \frac{\sum_p p^2 n_p S_p(q)}{\sum_p p^2 n_p S_p(q) R_{h,p}^{-1}} \qquad\qquad (3.29)$$

where $R_{h,s}'$, $R_{h,p}$ are the corresponding hydrodynamic radii of the oligomers of mass s and aggregates of mass p, and $S_p(q)$ represents the structure factor of the aggregates of mass p, and

$$I(q) = K'\left(m_0^2 \sum\nolimits_s s^2 o_s + M_C^2 \sum\nolimits_p p^2 n_p S_p(q)\right) \qquad (3.30)$$

In figure 8 we show the trends of the simulated hydrodynamic radius obtained from (3.27) using (3.29) evaluated at q=193000 cm^{-1}, and considering the first monomer $o_1(t)$ of 10 nm radius. The extended expressions for $K_{i,j}^N$ and $K_{i,j}^A$ used are the sequent:

$$K_{ij}^N = \frac{W_N^{-1} K_B}{4}(i^{-\frac{1}{3}} + j^{-\frac{1}{3}})(i^{\frac{1}{3}} + j^{\frac{1}{3}})(ij)^{0.4}$$
$$K_{ij}^A = \frac{W_A^{-1} K_B}{4}(i^{-\frac{1}{2.05}} + j^{-\frac{1}{2.05}})(i^{\frac{1}{2.05}} + j^{\frac{1}{2.05}})(ij)^{0.4} \qquad (3.31)$$

With $k_N = W_N^{-1} K_B$, ranging from 10^{-6} to 10^{-3} and $k_A = W_A^{-1} K_B = 10^{-4} s^{-1}$.

Therefore, in this simulation we consider both the aggregation and the nucleation process as an RLCA kinetic, but the structure of the critical nucleus is an hard sphere (d_f=3), and the structure of aggregates is a typical RLCA fractal structure (d_f=2.05).
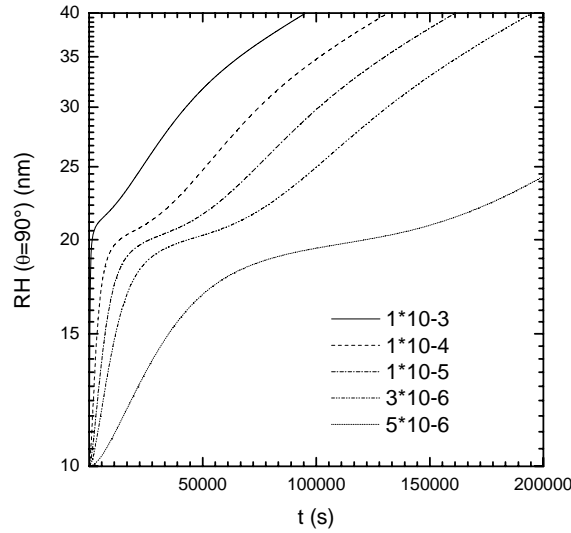

FIGURE 8.   simulated hydrodynamic radius obtained from the resolution of (3.34) using the expression (3.11) evaluated at q=193000 cm^{-1}, and considering the first monomer $o_1(t)$ of 10 nm radius. The values for k_N range from 10^{-5} to 10^{-3} and $k_A = 3*10^{-6} s^{-1}$.

The solutions shows that the hydrodynamic radius has a first rapid growth, coincident with the critical nucleus formation, followed by a slower growth phase, exponential, during which the preformed nuclei start to aggregate.

There are two visible effects in maintaining the aggregation rate fixed while varying the nucleation rate: the first is that growth becomes slower as the nucleation rate is decreasing, and consequently the lag time τ increases. The second is that, although the aggregation rate is constant, the second growth phase become slower. This means that the nucleation rate has an important effect on the growth rate of the aggregates.

In the Figure 9(a) we show the same solutions but with k_A ranging from 10^{-5} to 10^{-3} and $k_N = 3*10^{-6} s^{-1}$.
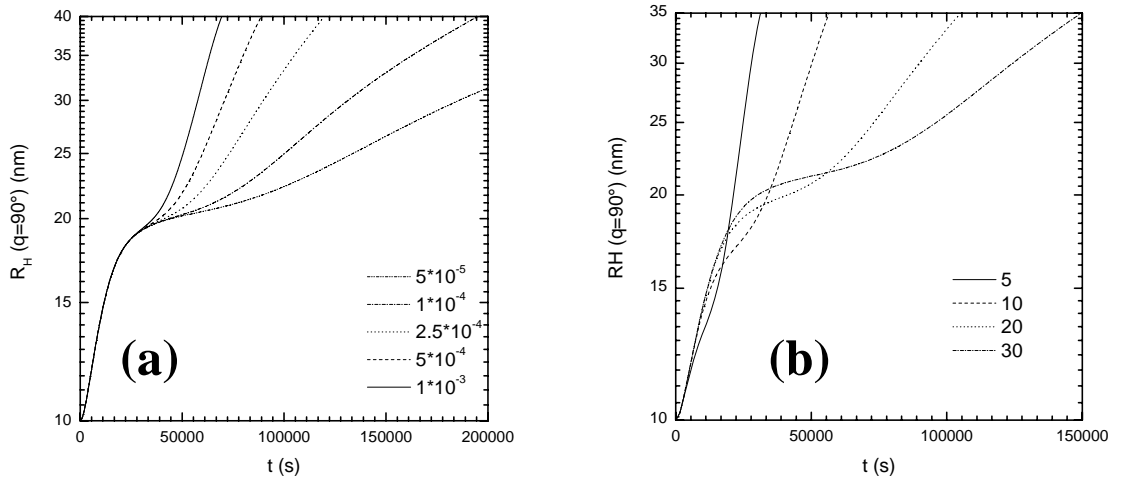

FIGURE 9. (a) simulated hydrodynamic radius obtained from the resolution of (3.34) using the expression (3.11) evaluated at $q=193000$ cm^{-1}, and considering the first monomer $o_1(t)$ of 10 nm radius. The values for k_A range from 10^{-5} to 10^{-3} and $k_N = 3*10^{-6} s^{-1}$. (b) simulated hydrodynamic radius obtained from the resolution of (3.34) using the expression (3.11) evaluated at $q=193000$ cm^{-1}, and considering the first monomer $o_1(t)$ of 10 nm radius. The values used in the nucleation and aggregation frequency function are $k_A = 2.5*10^{-4}$ and $k_N = 3*10^{-6} s^{-1}$, and the values of Nc are 5, 10, 20, 30.

In this case we observe that maintaining the nucleation rate fixed, the aggregation rate, as expected, has no effect on the first growth step.

In figure 9 (b) we show the solutions with $k_A = 2.5*10^{-4} \ s^{-1}$ and $k_N = 3*10^{-6} s^{-1}$, for different values of Nc: increasing the Nc value means to increase the lag time and to decrease the aggregation rate, because the overall nucleation process become slower.

4. Kinetics of nucleation-aggregation in α-crystallin suspensions

4.1 Introduction

In section 3.4.1 we related the measurable quantities of light scattering to those calculated from the cluster mass distribution (CMD), which is the solution obtained from the PBE. In this chapter, we develop a procedure that allows a significantly improved discrimination among different kinetics models, since we actually include information about the distribution width and shape by considering two different averages of the distribution.

The developed procedure will be used to characterize heat and Ca^{2+}-induced kinetics of nucleation and aggregation of α-crystallin. Surprisingly, we find evidence that α-crystallin exhibits a temperature-dependent self-chaperone effect, that preserves the lens from a premature opacification by delaying the aggregation of denatured crystallins in hypertermic and stressful conditions. A possible mechanism explaining this effect is given, based on available experimental data.

4.2 Experimental section

4.2.1 Experimental techniques

Scattering techniques, involving radiation sources like neutrons, x-rays and light, are probably the most widely used to characterize colloidal systems and soft condensed matter in general (Linder, 2002). The particular application used in this work is light scattering, because it is a non-invasive technique and the wavelength range is ideal to gain structural informations from the mesoscopic systems (1 nm÷1 µm) on which we are interested. More generally, light scattering is due to the interactions of electromagnetic waves with matter and its dielectric properties (Klein, 1996).
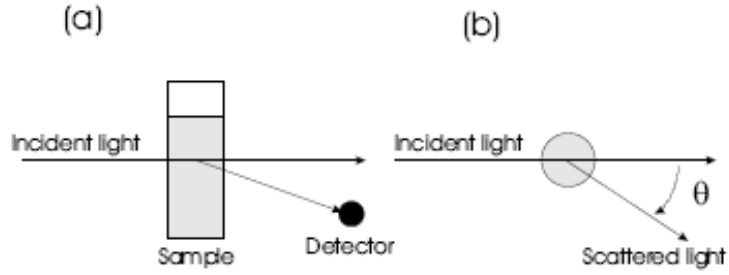

FIGURE 10. Schematic of a scattering experiment. (a) side view, (b) top view.

 An important development in the theory of light scattering, greatly simplifying its analysis and applicability, is the Rayleigh-Debye-Gans theory (Kerker, 1969). This RDG theory is limited to single scattering and assumes that the incoming light is greatly unaffected by the scattering particles. The conditions for which the RDG theory is applicable are

$$(4\pi R_p / \lambda_0) \left| \frac{n_p}{n_s} - 1 \right| << 1 \qquad (4.1)$$

where R_P is the radius of a particle, λ_0 the wavelength of the incident light and n_p and n_s the refractive indices of the particle and the solvent, respectively. If these conditions do not hold, it is still possible to use the however more complex Mie theory (Kerker, 1969).

In a typical light scattering experiment, a monochromatic laser is directed onto the centre of a sample and the light scattered in the horizontal plane is collected as a function of the angle formed with the direction of the primary beam, as depicted schematically in Figure 10. Two different experiments can be performed with this set-up. In a static light scattering experiment (SLS), the time averaged scattered intensity is measured as a function of the scattering angle and provides useful information about the spatial structure of the sample under investigation. In the case of aggregates of primary particles we can learn how these particles are distributed within the clusters. However, it is important to note that SLS always provides an average information, i.e. the signal obtained is an average over all the different shapes and sizes of the particles and clusters present in the sample. This is the reason why an interpretation of SLS data requires considerable care and a detailed model. The same holds true for the second technique, dynamic light scattering (DLS), in which the temporal fluctuation of the scattered intensity is analyzed with correlation schemes (Berne and Pecora, 1976; Brown, 1996).
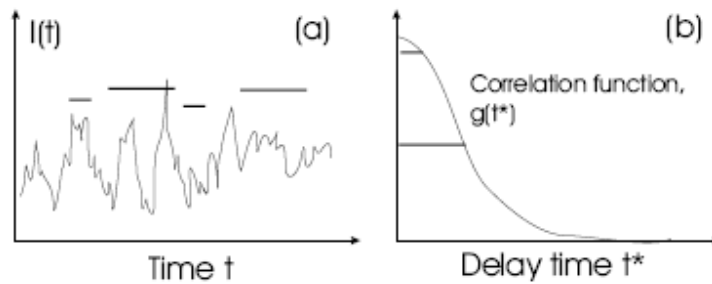
FIGURE 11. Schematic of DLS: (a) intensity fluctuations. (b) Correlation function obtained from the intensity fluctuations as a function of the delay time t[*]

In this analysis the fluctuations at a certain time t are correlated to a time shifted by a certain delay time constant t^*. If the signal at these two times is correlated, a certain nonzero value is obtained for this delay time interval t*. If particles have not moved at all in this time interval, the correlation value is one. In case the particles have moved significantly and have erased all correlations between their positions at the initial time and the delay time, a value of zero is obtained. This is shown schematically in Figure 11. Conceptually, DLS measures how fast a particle (or another object of interest) diffuses away from its original position. This can be related to an effective diffusion coefficient and therefore to an effective hydrodynamic radius. As in SLS, in DLS we always obtain values which are averages over all particle sizes and shapes. Further relevant details will be given in the following subsections.

4.2.1.1   Static light scattering

Static light scattering (Kerker, 1969) measures the time-averaged intensity $I(q)$ scattered from a sample as a function of the scattering wave vector:

$$q = \frac{4\pi n}{\lambda_0} sen\left(\frac{\vartheta}{2}\right) \qquad (4.2)$$

where λ_0 is the incident light wavelength, n is the refractive index of the solution, and θ is the scattering angle.

The measured scattering intensity from aggregating particles can be written as:

$$I(q) \propto \sum_M m^2 n(m) S_i(q) P(q) \qquad (4.3)$$

where the contribution $M^2 S(qR_G)$ from a single cluster of mass M and radius of gyration R_G is weighted over cluster-mass distribution $N(M)$, and $P(q)$ is the form factor of the primary particle. The structure factor S of the aggregates can be obtained analytically by Fourier transforming the pair-correlation function of fractal objects (Chen and Teixeira, 1986). Its normalized form with $S(0) = 1$ is given by the equation:

$$S_i(q) = \left(1 + \frac{2}{3d_f}(qR_{g,i})^2\right)^{-\frac{d_f}{2}} \qquad (4.4)$$

where the dependence on the product qR_G only follows the scale invariance of the cluster. Two asymptotic behaviours of the structure factor, corresponding to different experimental conditions, can be found during aggregation:

$$S_i(q) \propto \begin{bmatrix} 1 & qR_g \ll 1 \\ (qR_g)^{-d_f} & qR_g \gg 1 \end{bmatrix} \qquad (4.5)$$

When clusters can be considered like point sources, i.e., $qR_G \ll 1$, static light-scattering intensity measurements can be used to determine the time evolution of the average cluster mass: $I(t) \propto \sum_m n(m)m^2 = \bar{M}$. When most clusters are large enough to have $qR_G \gg 1$, the fractal dimension d_f can be directly determined by measuring scattered intensity versus wave vector q: $I(q) \propto q^{-d_f}$. In the cross-over region $qR_G \sim 1$, the full expression (4.3) must be used.

4.2.1.2 Dynamic light scattering

Dynamic light scattering (Berne and Pecora, 1976) measures the time autocorrelation function of the scattering intensity $I(t)$. The normalized autocorrelation function is defined as:

$$G_2(\tau) = \frac{\langle I(0)I(t)\rangle}{\langle I\rangle^2} \qquad (4.6)$$

where τ is the delay time and the angular brackets indicate the ensemble average.

The time dependence of the scattered intensity results from local density fluctuations as a consequence of the diffusive motion of the clusters. The autocorrelation function of these density fluctuations $g_1(t)$ can be derived from G_2 using the Siegert relation:

$$G_2(\tau) = 1 + Bg_1(\tau)^2 \qquad (4.7)$$

where B is an instrumental constant.

For monodisperse point particles, the density autocorrelation function decays exponentially in time as $g_1(\tau) = e^{-\Gamma \tau}$, where the decay rate Γ depends on the particle translational diffusion coefficient according to $\Gamma = Dq^2$. In the case of aggregating particles, deviations from the monoexponential decay are observed because of cluster polydispersity and rotational diffusion effects.

In this condition, the derivative of g_1 for $t \to 0$ measures the average decay rate of the clusters:

$$\langle \Gamma \rangle = \left. \frac{\partial \ln g_1(t)}{\partial t} \right|_{t=0} \qquad (4.8)$$

To determine $\bar{\Gamma}$ experimentally, we fitted the logarithm of the measured autocorrelation function g_1, to a third-order polynomial, according to the cumulant expansion (Koppel, 1972):

$$\ln g_1(t) = -\Gamma_1 t + \frac{1}{2!} \Gamma_2 t^2 - \frac{1}{3!} \Gamma_3 t^3 + o(t^4) \qquad (4.9)$$

Where we assumed $\langle \Gamma \rangle = \Gamma_1$.

In aggregating systems, because of cluster-mass polydispersity, what we actually measure is an average effective diffusion coefficient that can be expressed as:

$$\langle D_{eff} \rangle = \frac{\bar{\Gamma}}{q^2} = \frac{\sum_m n(m) m^2 S(qR_G) D_{eff}}{\sum_m n(m) m^2 S(qR_G)} \qquad (4.10)$$

The average effective hydrodynamic radius $<R_{h,eff}>$ can be obtained using Einstein Relation

$$< R_{h,eff} > = \frac{k_B T}{6\pi\eta < D_{h,eff} >} \qquad (4.11)$$

4.2.2   Experimental procedures

4.2.2.1   Light scattering.

Static and dynamic light-scattering measurements were performed concurrently during α-crystallin aggregation by using a computer-interfaced scattering system ALV-125 (ALV GmbH, Langen, Germany). A vertically polarized monochromatic light source at 632.8 nm produced by an NEC He-Ne 50 mW laser was used. The sample was contained in a cylindrical quartz cuvette (1-cm diameter) enclosed in a vat filled with toluene as optical matching fluid. Sample temperature was controlled within ± 0.01°C by means of a Julabo HC Thermostat and measured with a Ptl00 thermometer. Photons scattered by the sample were revealed by a single photon photomultiplier mounted on the rotating arm of the goniometer.

The photopulses were sent to a 256-channel digital autocorrelator (ALV-5000) that performed a hardware autocorrelation function of the photopulses with a logarithmic spacing of delay times starting from 0.2 μs. Counts per second were used to measure the scattered intensity during the aggregation.

Data were collected from several scattering angles (usually eight) ranging from 30° to 150°, corresponding to wave vectors $0.46*10^5 < q < 2.5*10^5$ cm^{-1}. Because the measurements were performed during the aggregation process, data are a function of both scattering vector q and aggregation time t. The slow rate of the α-crystallin aggregation and the high values of scattered intensity usually allowed an average collecting time of 30 s, sufficient to obtain a good measure of the intensity autocorrelation function before the system could change significantly.

4.2.2.2   Preparation of α-crystallin suspensions

α-crystallin from bovine eye lens was prepared according to Santini et al. (Santini, 1992). The α-crystallin fractions suspended in 10 mM Tris-HCl buffer, pH 7.4, were thoroughly mixed and pooled together. The purified protein was divided into aliquots and kept in the same buffer at -20°C until used. Just before the experiment, the samples were thawed and centrifuged at 50, 000 x g for 30 min at 4°C, and the supramolecular aggregates already formed were discarded. The supernatant was filtered through a 3-mm Millipore low-retention filter (0.2 μm pore diameter) directly into the measuring cuvette. Protein   concentration was determined by using an absorption coefficient of A=0.81 at 280 nm (Delaye and Gromiec, 1983).

4.3   Experimental results

4.3.1 Temperature dependence of nucleation and aggregation kinetics

Heat and Ca^{2+} induce α−Crystallin aggregation. In particular, heat modifies the quaternary structure of the proteins, and Ca^{2+} decreases the thermal stability of α-crystallin by promoting partial unfolding of the protein(see chapter 2).

To further investigate the effect of the temperature and of the phase transition near *Tc*=318.16 K we followed growth kinetics at different temperatures in the range 310÷330 K by means of static and dynamic light scattering, while maintaining the protein concentration ([α]=1 mg/ml) and Ca^{2+} concentration ([Ca^{2+}]=16mM) fixed in 10 mM Tris-HCl buffer, pH 7.4.
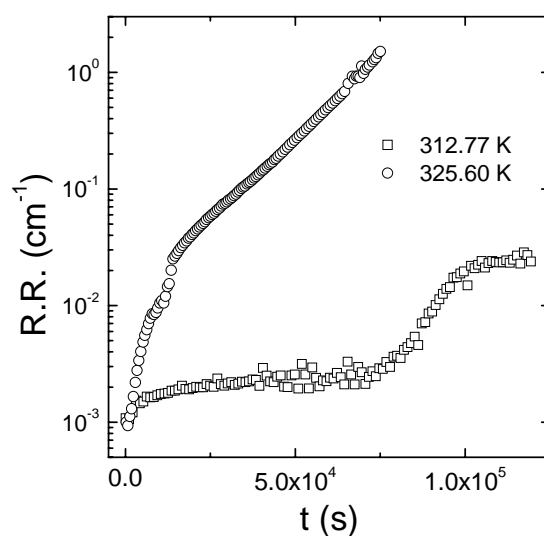
FIGURE 12 Rayleigh Ratios measured at θ=90° versus aggregation time t of 1.0 mg/ml a-crystallin in 10 mM TRIS-HCI buffer, pH 7.4, with 16 mM CaCl2 at 312.77 K and 325.10 K.

In Figure 12 Static light scattering intensities of α-crystallin measured at θ=90° versus aggregation time *t* are reported at two different temperatures 312.77 K (below *Tc)*, and 325.10 K (above *Tc)*.

Both kinetics appear to be governed by a two step mechanism. The kinetics at 325.10 K in the first phase, lasting 10000 s, is characterised by a fast enhancement of scattering intensity (Fig. 12). Later on, the scattering intensity slows down to an exponential increase. These findings well agree with previous measurements performed by our group (Andreasi Bassi et. Al, 1995).

In the kinetics at 314.45 K (below *Tc)*, the rate of the two steps appears inverted: the intensity undergoes an initial rapid increase followed by a lag phase, and then abruptly grows up in an exponential way since a plateau is reached.

These qualitative characteristics of growth kinetics are maintained also when extending measurements at different temperatures in the range 310÷330 K. In Figure 13a static light scattering intensities measured at θ=90° versus aggregation time *t* are reported at different temperatures above *Tc*, and in figure 13b, below *Tc*.
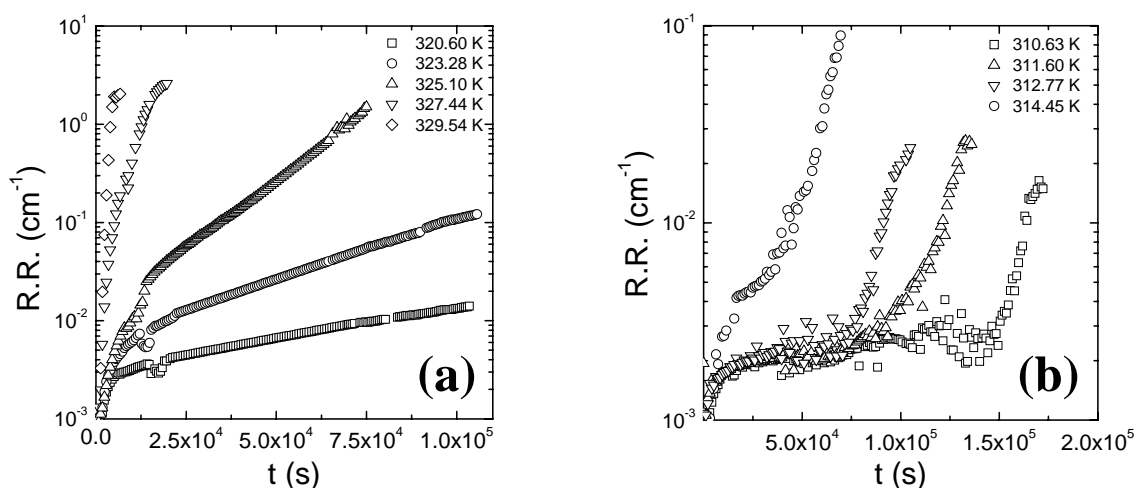
54

FIGURE 13 (a) Rayleigh Ratios measured at θ=90° versus aggregation time t of 1.0 mg/ml a-crystallin in 10 mM TRIS-HCI buffer, pH 7.4, with 16 mM CaCl2 at 310.63 K, 311.60 K, 312.77 K and 314.45 K, above *Tc*. (b) Rayleigh Ratios versus aggregation time t of 1.0 mg/ml a-crystallin in 10 mM TRIS-HCI buffer, pH 7.4, with 16 mM CaCl2 at 320.6 K, 323.28 K, 325.10 K, 327.44 K and 329.54 K, below *Tc*.

We see in figure 13b that, below *Tc*, the lag phase decreases as the temperature increases. Above *Tc* (fig.13a) at 320.6 K the overall process is slowed down abruptly, and the first and second phase of aggregation are completely overlapped. Raising the temperature further leads to an increase of both rates of the process.

After the first step, the scattering intensity shows an exponential increase at all the temperatures investigated. In order to obtain further information about the aggregation kinetics and the cluster dimension, both independent of and related to static light scattering, dynamic light scattering measurements were performed on the same data.
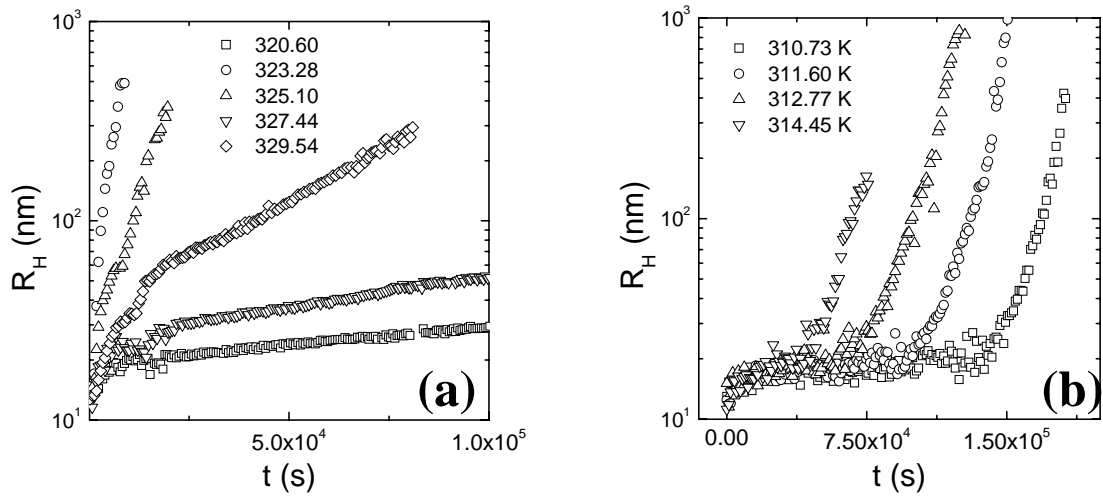
FIGURE 14 (a) Hydrodynamic radius versus aggregation time t of 1.0 mg/ml a-crystallin in 10 mM TRIS-HCl buffer, pH 7.4, with 16 mM CaCl2 at 320.6 K, 323.28 K, 325.10 K, 327.44 K and 329.54 K, above Tc. (b) Hydrodynamic radius measured at $\theta=90°$ versus aggregation time t of 1.0 mg/ml a-crystallin in 10 mM TRIS-HCl buffer, pH 7.4, with 16 mM CaCl2 at 310.63 K, 311.60 K, 312.77 K and 314.45 K, below Tc.

Fitting the autocorrelations function $g_1(t)$ measured at 90° (q=0.0186 nm^{-1}) using the cumulants method (equation 4.9), is conducive to the determination of the temporal evolution of the mean hydrodynamic radius $<R_{h,eff}(t)>$.   As we can see in Fig. 14, These temporal evolution are well-related with the scattered intensity growth kinetics. At temperatures above Tc (Fig.14a) there is a rapid initial growth of the hydrodynamic radius from 10 nm to around 20-30 nm, that is followed by an exponential growth, with a rate increasing with temperature. Again below Tc (Fig.14b) we found a lag-phase, decreasing with temperature, in which the radius value is stabilized around 20 nm. These lag phases are then followed by a very rapid growth.

In order to gain deeper structural insights, we can combine both SLS and DLS data. In Figure 15a angular scattered intensity distributions $I(q)$ are reported at the latest stages of the aggregation at 325.60 K.
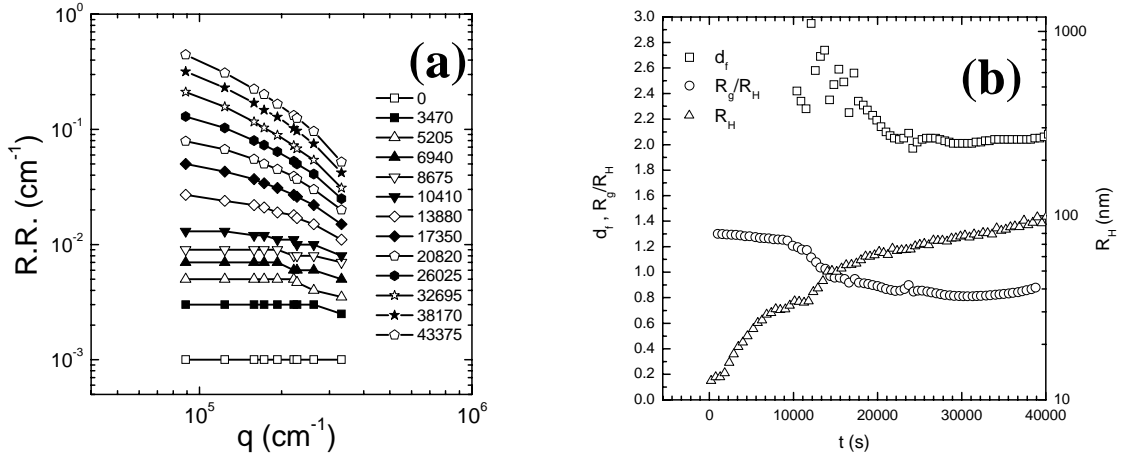
FIGURE 15   (a) Rayleigh Ratios versus wave vector q at different aggregation times t. Concurrent values at each q were obtained by interpolating from the data plotted in Fig. 1. Solid lines represent the dependence on q of the function used to fit the experimental data. (b) Values of the *df, Rh* vs time and the *Rg/Rh* ratio versus time.

The experimental data were henceforth fitted according to the nucleation-aggregation model. Following section 3.4, the monomers o_1, having mass m_0, react with each other as well as with different size oligomers so as to become larger clusters, as long as a condition with minimum Gibbs free energy corresponding to the size of a cluster o_f (or nucleus), $M_C = N_c m_0$ persists. Any aggregates larger than the cluster would convert into the basic unit of the aggregation. With this assumption, indicating with $o_s(t)$ the number of the growing oligomer of mass $m = s\, m_0$ at time t and indicating with $n_p(t)$ the number of the aggregates of mass $m = p\, M_C = p\, N_C m_0$ at time t the experimental scattered intensity is described by

$$I = K\left(\sum_s o_s s^2 P(qR_s) + N_c^2 \sum_p n_p p^2 P(qR_C) S_p(q)\right) \qquad (4.13)$$

Where the first term on the left represents the intensity scattered by the nucleating monomers, the second term represents the intensity scattered by the clusters whose basic unit is the critical nucleus *Rc*. $P(qR_i)$ is the form factor for a sphere with radius R (Kerker, 1979):

$$P(qR_i) = \left[\frac{3\left(sen(qR_i) - qR_i \cos(qR_i)\right)}{(qR_i)^3} \right]^2 \qquad (4.14)$$

And S(q) is given by the (4.4).

In the first stages of aggregation we can consider a near monodisperse mass distribution and (4.13) then reduces to the very simple form

$$I = AP(q\langle R \rangle) + BP(qR_C)S(q\langle R_g \rangle) \qquad (4.15)$$

Where $\langle R \rangle$ is the mean radius of the nucleating oligomers and $\langle R_g \rangle$ is the mean gyration radius of the aggregates.

Using (4.15) also in the late steps of aggregation as opposed to the full form factor (4.4), would imply that we are considering the monodisperse mass distribution as in a DLCA process, which is clearly not our case. But we already demonstrated that the fitting parameter d_f does not change significantly (Andreasi, 1995). The robustness of the d_f demonstrates straightforwardly the sensitivity of static light scattering in determining the internal structure of the clusters.

In figure 15(b) we report the values of the d_f, $\langle R_H \rangle$ and $\langle R_H \rangle / \langle Rg \rangle$ ratio during the first stages of aggregation at T=325 K, determined by fitting the experimental data with (4.15).

In the first growth phase, i.e. for the first 10000 s, the ratio $\langle R_H \rangle / \langle Rg \rangle$ is constant, and his value is 1.28, which is nearly the value of a sphere (Lattuada, 2003). Only after this plateau the ratio $\langle R_H \rangle / \langle Rg \rangle$ starts to decrease with time, reaching the asymptotic limit typical of the RLCA (0.831). At the same time, the fractal dimension d_f stabilizes its value at 2.05.

The first step could be ascribed to an initial nucleation process, consisting in the conversion of the protein from the native to the heat and calcium-induced conformers and to their consequent binding into high molecular weight species (HMW, see chapter 3). The second step could be ascribed to the subsequent aggregation of the HMWs, identified with the critical nuclei of the aggregation. We have found the same structural features at all the other temperatures.

4.3.2 Ca^{2+} dependence of nucleation and aggregation kinetics

In figure 16 we show the effect of the Ca^{2+} concentration on the growth kinetics, above and below *Tc*. In figure 16a, we observe the Hydrodynamic radii at 325.12 K, above *Tc*, at different [Ca^{2+}], from 4mM to 64mM.
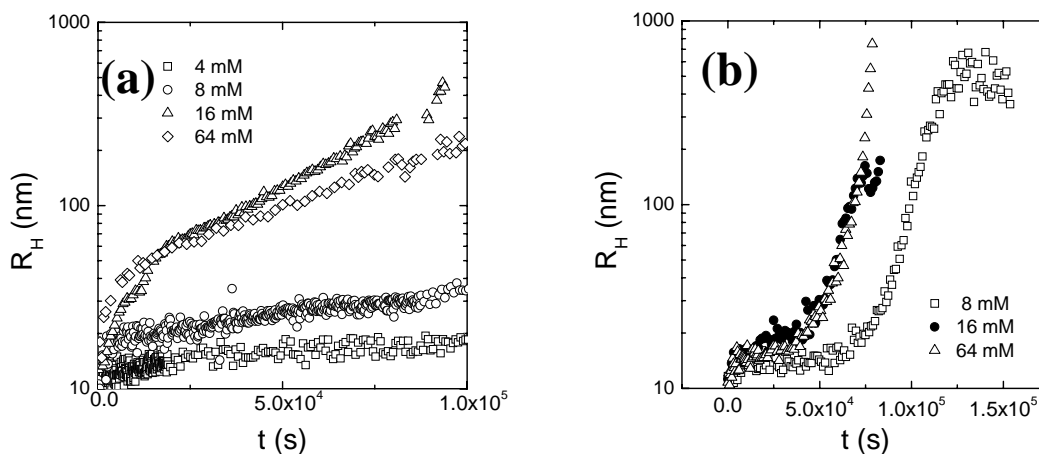

FIGURE 16   (a) Hydrodynamic radius measured at θ=90° versus aggregation time t of 1.0 mg/ml α-crystallin in 10 mM TRIS-HCI buffer, pH 7.4, the Hydrodynamic radii at 325.12 K, above *Tc*, at different [Ca^{2+}] (4mM, 8mM, 16 mM, 64 mM). (b) Hydrodynamic radius measured at θ=90° versus aggregation time t of 1.0 mg/ml a-crystallin in 10 mM TRIS-HCI buffer, pH 7.4, the Hydrodynamic radii at 314.16 K, below *Tc*, at different [Ca^{2+}] (8mM, 16 mM, 32 mM)

By increasing [Ca^{2+}] the first rapid growth seems to increase its rate. Also the second exponential growth increases its rate from 4mM to 32 mM, but at 64 mM there is a slight inversion of this trend.

A similar behaviour is noted in the measurements made at 314.45 K, below T_c. From 8 mM to 16 mM the lag time decreases but, increasing [Ca^{2+}] further, no substantial changes in the kinetics occur.

4.3.3 Concentration dependence of nucleation and aggregation kinetics

We also monitored, below Tc, the lag time trend in respect to the protein concentration. We observe in figure 16a the Hydrodynamic radii at 314.45 K, at different [α], from 0.3 mg/ml to 14 mg/ml.

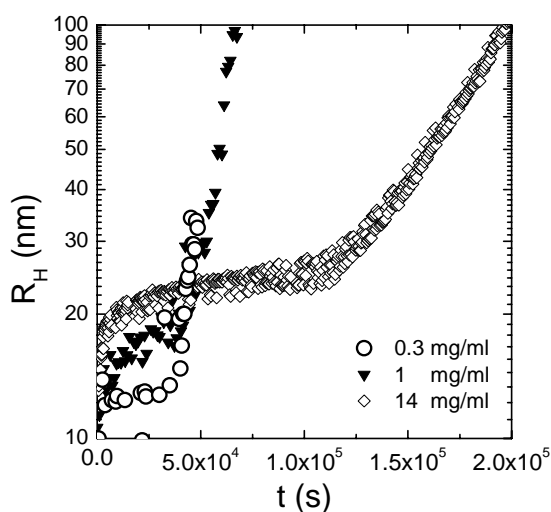
FIGURE 17   Hydrodynamic radius measured at θ=90° versus aggregation time t of a-crystallin in 10 mM TRIS-HCI buffer, pH 7.4, at 314.45 K, below Tc, at different [a], from 0.3 mg/ml to 14 mg/ml

We can see in figure 17 that the increase of concentration of the protein has as a main effect the increase in the nucleation rate .

4.4 Discussion

4.4.1 Determination of nucleation and aggregation rates

As we have seen in section 3.4.1, we can compare the experimentally accessible quantities as $I(q)$ and $<R_{h,eff}>$ with those computed from the cluster mass distribution n_i according to the nucleation-aggregation process.

In this chapter, we develop an iterative procedure that, combining SLS and DLS data, namely $I(q)$ and $<R_{h,eff}>$, allows us to discriminate among different kinetic models. Indeed, by using kinetics evolution of both $I(q)$ and $<R_{h,eff}>$ in the computation of PBE equations, we can account for two different averages of the distribution and we actually include information about the distribution width and shape. In order to compute $I(q)$ and $<R_{h,eff}>$, we need to know the structural features of the aggregates forming in the nucleation and in the aggregation process. During the initial growth, ascribed to the nucleation process, the particles have a spherical shape. The second step, corresponding to the aggregation process, brings to the formation of clusters having a random fractal shape of dimension d_f=2.05. In summary, the nucleation process leads to the formation of a critical nucleus that is an hard sphere ($d_{f,\,nuc}$=3), and it is followed by an aggregation process that proceeds accordingly to a RLCA (d_f =2.05). Basing on these structural features, substituting (3.8) in (3.30), we will have for $I(q)$:

$$I(q) = K'\left(m_0^2 \sum_s s^2 o_s + M_C^2 \sum_p p^2 n_p \left(1 + \frac{2}{3d_f}(qR_{g,p})^2 \right)^{-\frac{d_f}{2}} \right) \qquad (4.16)$$

with the $R_{g,\,p}$ given by the relation (3.15) and d_f=2.05.

In order to compute $<R_{h,eff}>$, substituting (3.8) in (3.29), we will have:

$$< R_{h,eff} >= \frac{\sum_s s^2 o_s}{\sum_s s^2 o_s \left(R'_{h,s}\right)^{-1}} + \frac{\sum_p p^2 n_p \left(1+\frac{2}{3d_f}(qR_{g,p})^2\right)^{-\frac{d_f}{2}}}{\sum_p p^2 n_p \left(1+\frac{2}{3d_f}(qR_{g,p})^2\right)^{-\frac{d_f}{2}} R_{h,p}^{-1}} \qquad (4.17)$$

With d_f=2.05, the $R_{g,\,p}$ given by the relation (3.15), the $R_{h,\,p}$ given by the relation (3.14), the $R'_{h,s}$ given by the relation (3.3) with d_f=3. Accordingly, the nucleation frequency function and the aggregation frequency function, $K_{i,j}^N$ and $K_{i,j}^A$, are

$$K_{ij}^N = W_N^{-1} K_B \frac{1}{4}(i^{-\frac{1}{d_{f,nuc}}} + j^{-\frac{1}{d_{f,nuc}}})(i^{\frac{1}{d_{f,nuc}}} + j^{\frac{1}{d_{f,nuc}}})(ij)^{\lambda_0} \quad with \ d_{f,nuc} = 3, \lambda_0 = 0 \qquad (4.18)$$

$$K_{ij}^A = W_A^{-1} K_B \frac{1}{4}(i^{-\frac{1}{d_f}} + j^{-\frac{1}{d_f}})(i^{\frac{1}{d_f}} + j^{\frac{1}{d_f}})(ij)^{\lambda} \quad with \ d_f = 2.05, \lambda = 0.4 \qquad (4.19)$$

that are the principal input of the PBE (3.34).

By means of non-linear least squares algorithms, we can finally determine the crucial parameters Nc, $K_{nuc} = W_N^{-1} K_B$ and $K_A = W_A^{-1} K_B$. K_{nuc} represents the rate of formation of the first dimer in the nucleation process: indeed, (4.18) is $W_N^{-1} K_B$ for i=1 and j=1. It should be noted that it is also possible to recover all the other rate constants (i.e. monomer-dimer, dimer-tetramer) from (4.18). A similar argument holds for K_A, which represents the rate of dimerization of two critical nuclei. All the other related rate constants can also be obtained from (4.19)

The iterative fitting procedure consists of:

1) fitting of *I(q)*, which leads to the estimation of the three unknown parameters.

2) The parameters determined are used as starting guess for the fit of $< R_{h,eff}(q) >$.

3) If, after minimization, the parameters variation between the first and the second fitting procedure is less than 5%, the kinetic model is considered well in agreement with the experimental data.

4) If, after minimization, the parameters variation between the first and the second fitting procedure is more than 5%, other aggregation

frequency function parameters like λ, λ_0, $d_{f,\,nuc}$, d_f are automatically varied, and the procedure restarts from point 1.
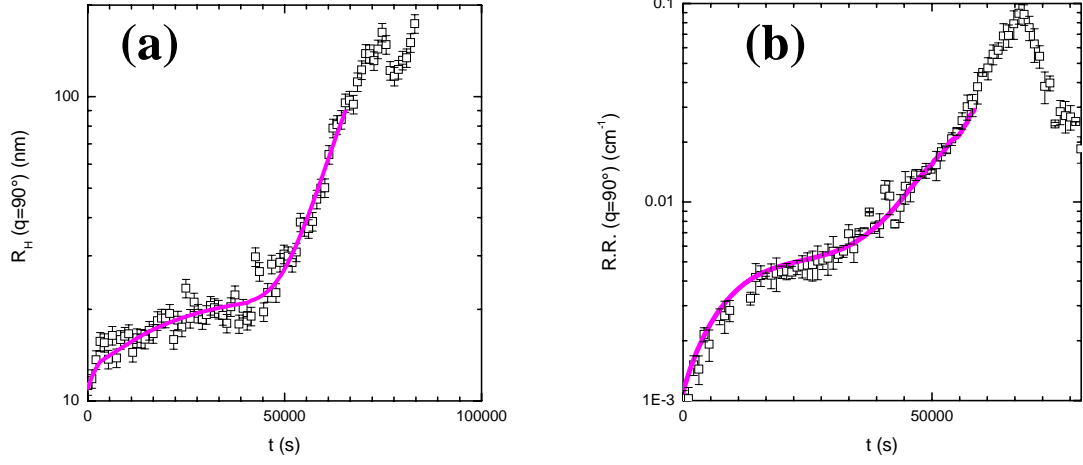

FIGURE 18   (a) Hydrodynamic radius measured at $\theta=90°$ versus aggregation time t of 1.0 mg/ml α-crystallin in 10 mM TRIS-HCI buffer, pH 7.4, at 314.45 K, below Tc. The solid line is the fit to the experimental data performed using the nucleation aggregation model developed in § 3.5. (b) Rayleigh Ratio measured at $\theta=90°$ versus aggregation time t of 1.0 mg/ml α-crystallin in 10 mM TRIS-HCI buffer, pH 7.4, at 314.45 K, below Tc. The solid line is the fit to the experimental data performed using the nucleation aggregation model developed in § 3.5.

In our case, for all the observed growth kinetics the values of these last parameters stabilize around the values reported in (4.18) and (4.19). This suggests that no variations to the functional forms of K_{ij}^N and K_{ij}^A occur in these different environmental conditions.

As an example, figure 18 shows the fit of eq. (4.16) to $I(q)$ (Fig.18a) and the fit of eq. (4.17) to $< R_{h,eff}(q) >$ (Fig.18b), measured at 314.45 K, below Tc. Figure 19 shows the same fits to $I(q)$ and $< R_{h,eff}(q) >$ measured at 325.60 K, above Tc.

It can be seen that (4.16) and (4.17) perfectly recover experimental data, which reinforces the view that the growth kinetics is a two step-process, a nucleation phase followed by an aggregation phase.
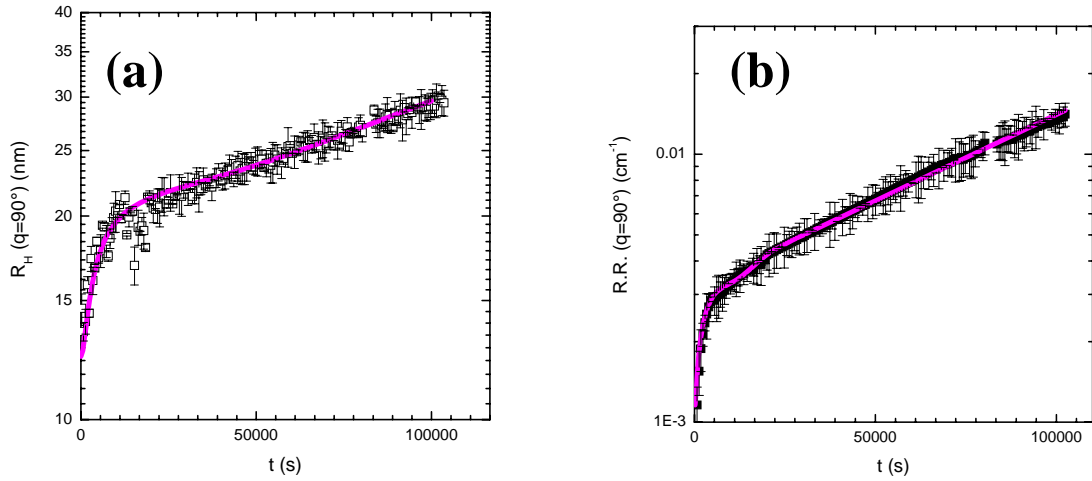
FIGURE 19   (a) Hydrodynamic radius measured at θ=90° versus aggregation time t of 1.0 mg/ml α-crystallin in 10 mM TRIS-HCI buffer, pH 7.4, at 325.60 K, above *Tc*. The solid line are the fit to the experimental data performed using the nucleation aggregation model developed in § 3.5. (b) Rayleigh Ratio measured at θ=90° versus aggregation time t of 1.0 mg/ml α-crystallin in 10 mM TRIS-HCI buffer, pH 7.4, at 325.60 K, above *Tc*. The solid line are the fit to the experimental data performed using the nucleation aggregation model developed in § 3.5.

This procedure was repeated for all the kinetics followed while varying temperature, [Ca^{2+}], [α]. The results are reported in table 3.

Table 3 K_{nuc}, K_A and Rc values obtained at different T, $[Ca^{2+}]$, $[\alpha]$. Rc was calculated from Nc using the (3.20).

T (K)	$[Ca^{2+}]$ (mM)	$[\alpha]$ (μM)	K_{nuc} ($s^{-1}M^{-1}$)	K_A ($s^{-1}M^{-1}$)	Rc (nm)
310.63	16	50	$1.07 \cdot 10^{-5}$	$7.53 \cdot 10^{-3}$	22.2
311.6	16	50	$2.18 \cdot 10^{-5}$	$8.39 \cdot 10^{-3}$	23.5
312.7	16	50	$2.93 \cdot 10^{-5}$	$1.15 \cdot 10^{-2}$	20.8
314.45	16	50	$5.08 \cdot 10^{-5}$	$1.02 \cdot 10^{-2}$	22.2
320.6	16	50	$1.06 \cdot 10^{-4}$	$8.53 \cdot 10^{-4}$	26
323.8	16	50	$2.15 \cdot 10^{-4}$	$5.31 \cdot 10^{-3}$	25.9
325.28	16	50	$3.05 \cdot 10^{-4}$	$8.06 \cdot 10^{-3}$	29.1
327.28	16	50	$6.27 \cdot 10^{-4}$	$4.01 \cdot 10^{-2}$	29.1
329.54	16	50	$1.02 \cdot 10^{-3}$	$1.57 \cdot 10^{-1}$	29.1
314.45	16	15	$1.08 \cdot 10^{-6}$	$2.13 \cdot 10^{-3}$	23.6
314.45	16	700	$2.04 \cdot 10^{-4}$	$4.09 \cdot 10^{-2}$	24.9
314.45	8	50	$9.17 \cdot 10^{-6}$	$4.31 \cdot 10^{-3}$	21.5
314.45	32	50	$9.79 \cdot 10^{-5}$	$2.02 \cdot 10^{-2}$	24.1
314.45	64	50	$9.06 \cdot 10^{-5}$	$2.09 \cdot 10^{-2}$	23.9
325.28	4	50	$2.20 \cdot 10^{-5}$	$7.56 \cdot 10^{-5}$	28.2
325.28	8	50	1.09E-04	6.02E-04	27.2
325.28	32	50	4.10E-04	1.55E-02	29.2
325.28	64	50	4.62E-04	9.01E-03	28.9

4.4.2 Thermodynamic behaviour of nucleation and aggregation rates:

evidence of a self-chaperone beahaviour of α-crystallin

In Fig. 20 we summarize the nucleation and aggregation rates reported in tab.3, at $[Ca^{2+}]$=16mM and $[\alpha]$=50μM, in a semilogarithmic plot as a function of inverse temperature.
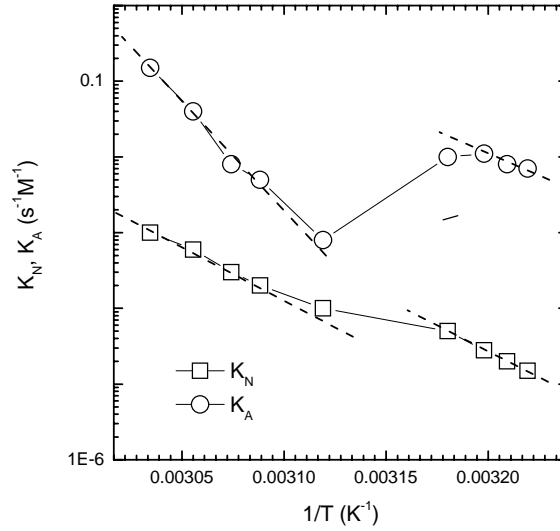
FIGURE 20   Arrhenius Plot of the aggregation and nucleation rates $K_{nuc} = W_N^{-1} K_B$ (squares), $K_A = W_A^{-1} K_B$ (circles).

Both rate constants exhibit an exponential trend till $1/T = 1/316$ K^{-1}: at this point they both abruptly break down, to then restart following the exponential trend with different slopes and prefactors. The jump between the two Arrhenius behaviours is in coincidence with the transition temperature of the quaternary structure of α-crystallin (Walsh, 1991).

The temperature dependence of the rate constants is assumed to follow the Arrhenius law in the regions where the exponential trends are detected (Lasaga, 1998),

$$k_A = A_{agg} \exp\left(-E_A^{agg}\Big/RT\right) \qquad (4.20)$$

$$k_N = A_{nuc} \exp\left(-E_A^{N}\Big/RT\right) \qquad (4.21)$$

Where A_{agg} A_{nuc} are prefactors and E_A^{agg} and E_A^{N} are respectively the energy of activation of formation of the first dimer in the nucleation process and the energy of activation of dimerization of the two critical nuclei.

In the two regions, the slopes of the straight line in Fig. 20 determine the activation energies below and above Tc, which are reported in table 4.

We may analyze the results obtained for both the nucleative and aggregative dimerizations in the framework of the transition state theory (Lasaga, 1998). We assume that one monomer can bind to the other only when it is inside a reaction volume v with a characteristic size $l \approx v^{\frac{1}{3}}$. We also assume that the monomers entering the reaction volume can actually bind to the other only if these monomers are in the appropriate activation state. The probability of the occurrence of such a state is $\exp(-\Delta G / k_B T)$, where ΔG is the change in free energy associated with the activation process. Thus the rate of dimerization can be written

$$k_D = \Gamma \exp\left(-\frac{\Delta G}{RT}\right) \qquad (4.22)$$

where Γ is the number of monomers entering the reaction volume per unit time. To estimate Γ, it must be noted note that the rate with which monomers enter a certain volume is equal to the rate with which they leave this same volume. The average number of monomers in a volume v at any moment of time is cv. These monomers are in a constant brownian motion and diffuse out of this volume in a time $\tau \approx l^2 / D \approx v^{\frac{2}{3}} / D$ to be replaced by others. Thus the number of monomers entering the reaction volume per unit time is cv/τ, and therefore

$$\Gamma \cong cv^{\frac{1}{3}} D \qquad (4.23)$$

It is reasonable to assume that the size of the reaction volume is of the order of the size of a monomer.

Substituting Eq. 4.23 into Eq. 4.22, and using the thermodynamic relation $\Delta G = E_A - T\Delta S$, where ΔS is the change in the entropy associated with the activation process, and comparing with Eq. 4.20, we have

$$k_D = cv^{\frac{1}{3}} D \exp\left(\frac{\Delta S}{R}\right) \exp\left(-\frac{E_A}{RT}\right) \qquad (4.24)$$

Eq. 4.24 permits a physicochemical interpretation of the significance of the parameters A and E_A, as obtained from the experimental measurements of $k_D(T)$. One can see indeed, by comparison of Eq. 4.24 and Eq. 4.22, that the activation entropy ΔS is related to the parameter A by

$$\Delta S = R\ln\left(\frac{A}{cv^{\frac{1}{3}}D}\right) \qquad (4.25)$$

In the case of the nucleation process the diffusion coefficient D (of the free monomer) is $3.6\ 10^{-7}\ cm^2/\sec^{-1}$ (for R_H= 10 nm). The reaction volume size $l = v^{\frac{1}{3}}$ is not well known. We may take it to be of the order of the dimension of the α-crystallin, namely 10 nm. Thus, we estimated the changes in the entropy associated with the activation process below and above Tc, namely $T\,\Delta S_N^{BT}$ and $T\Delta S_N^{AT}$, at 300 K, reported in table 4. In the case of the aggregation process, we can repeat the same calculus and the values of $T\,\Delta S_A^{BT}$ and $T\Delta S_A^{AT}$ at 300 K are still reported in table 4. Although the values used to calculate the activation entropy are not known accurately especially in this last case, even a factor of 10 uncertainty in the magnitude of $A/v^{\frac{1}{3}}$ introduces an error of only 2.7RT = 1.6 kcal/mol in $T\Delta S$, which is less then 4% of the total values. Note that, in comparison with the uncertainty in $v^{\frac{1}{3}}$, the error in the numerical value of A caused by a poorly known monomer concentration c produces an insignificant effect on the deduced value of the activation entropy ΔS.

In the table 4 are also reported changes in free energy associated with the activation processes, $\Delta G = E_A - T\Delta S$, calculated at 300 K

Table 4. Activation energies, activation entropies and activation free energies for the nucleation and aggregation process

	Nucleation			Aggregation		
	E_A (kcal/mol)	$T\Delta S$ (300K) (kcal/mol)	ΔG (kcal/mol)	E_A (kcal/mol)	$T\Delta S$ (300K) (kcal/mol)	ΔG (kcal/mol)
T<Tc	62.8	50.6	12.2	42.4	34.8	7.6
T>Tc	60.7	47.4	13.3	131.0	115.2	15.8

The free energies associated with the activation processes are of the order of 10 kcal/mol, which is a relatively small quantity, so that the probability for an activated state occurring, $\exp(\Delta G/RT) \approx 10^{-5}$, is sufficiently large for the reaction to take place within the observed rate. However, this small free energy results from the difference between the much larger activation energy and the entropy contribution, which goes from 40 to 130 Kcal/mol. The change in the free energy of activation with temperature, $\Delta\Delta G = \Delta G^{AT} - \Delta G^{BT}$, is 1.1 kcal/mol for the nucleation process and 8.2 Kcal/mol for the aggregation process. Below *Tc*, the free energy of activation of the nucleation process is nearly two times the free energy of activation of the aggregation process. Above *Tc*, while ΔG_N stays almost unchanged, ΔG_{Agg}^{AT}, the free energy of activation of the aggregation process above *Tc*, is nearly two times larger than ΔG_{Agg}^{BT}.

Therefore, the probability that an activated state occurs in the nucleation process is nearly the same above and below Tc, whereas the probability that an activated state occurs in the aggregation process switches from $\exp(\Delta G/RT) \approx 10^{-5}$ to $\exp(\Delta G/RT) \approx 10^{-11}$ at *Tc*. This delay in the aggregation of the crystallins would preserve the lens from a premature opacification in this hypertermic and stressful condition.
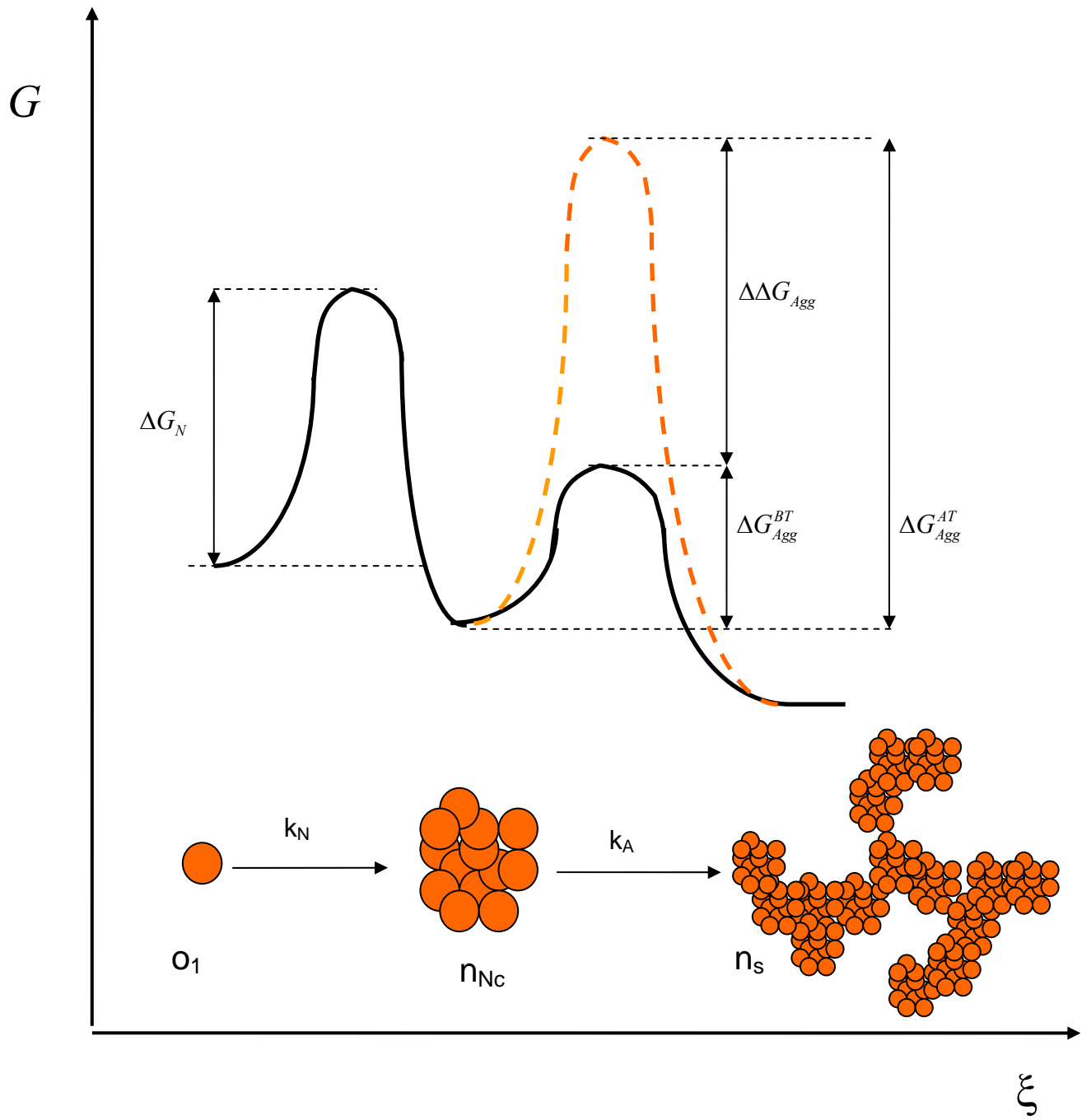
.

FIGURE 21. Schematic representation of the nucleation-aggregation process in a free energy landscape below and above *Tc*. The free energy is reported as function of a reaction coordinate ξ that represents the progress of the process. At each minimum corresponds a stable state. Values for ΔG_N, ΔG_{Agg}^{BT}, ΔG_{Agg}^{AT}, $\Delta\Delta G = \Delta G^{AT} - \Delta G^{BT}$ are graphically shown.

To gain further insights about this aspect, we would need to analyze the trend of the critical radius in function of temperature, reported in figure 22.
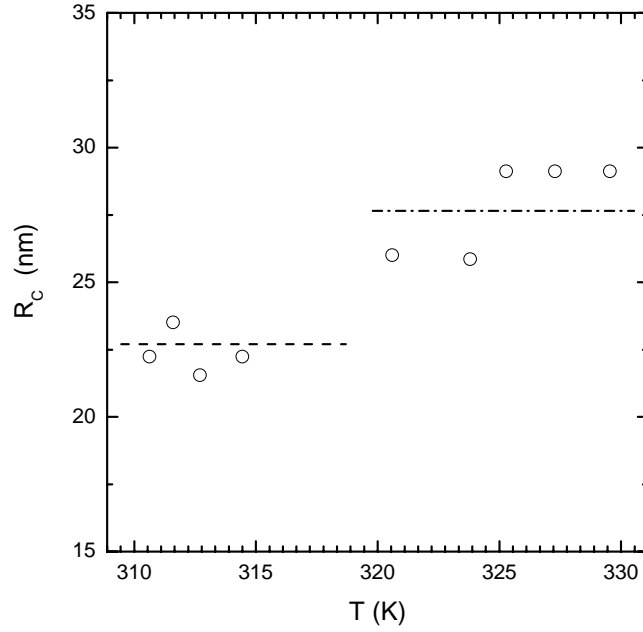
FIGURE 22. Critical Radius *Rc* in function of temperature. *Rc* was calculated from *Nc* using (3.20)

As it can be seen in correspondence of *Tc,* critical nuclei increase their radii from ~23 nm to ~28 nm. Above *Tc, Nc* is two times larger than below *Tc,* and we could estimate that the number of critical nuclei is near 1/2 of the number of critical nuclei below *Tc,* because the total mass is conserved and the nucleation rate does not vary appreciably. Thus, *Nc* increases, leading to the formation of a lesser number of critical nuclei.

Furthermore the activated states above and below *Tc* differ significantly in both energy and entropy, suggesting a substantial difference in structure. The energy difference we have quantified could be ascribed to more tight protein interactions. Indeed such a stabilization of the critical nucleus is evident when we estimate the protein-solution interfacial tension *γ,* above and below *Tc,* using (3.31) and (3.32) from the knowledge of *R** and *ΔG.*
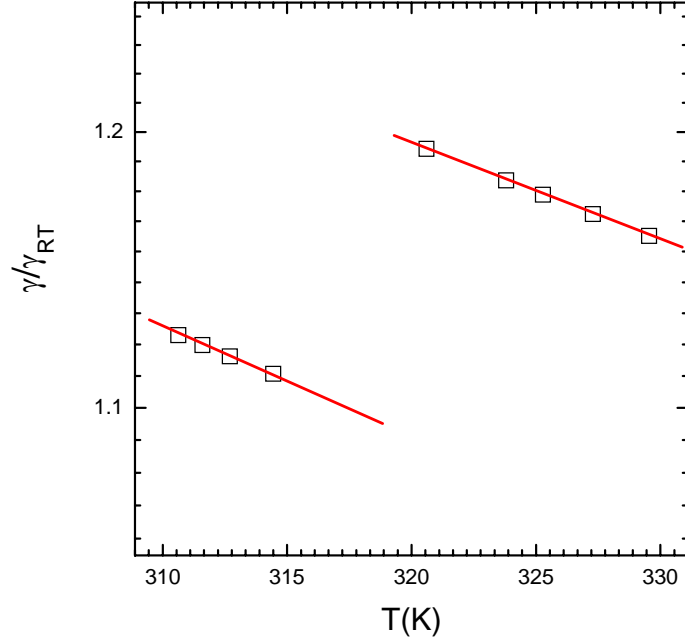
FIGURE 23. Ratio between the estimated γ, the protein-solution interfacial tension, and γ_{RT}, estimated considering a surface tension of RT over the area of a nucleus with critical radius Rc, in function of T.

In figure 23 we plot the γ/γ_{RT} ratio versus T, where γ is the estimated protein-solution interfacial tension, and γ_{RT} is the surface tension of RT estimated over the area of a nucleus with critical radius Rc. We observe a jump in the trend of γ/γ_{RT} in correspondence of Tc. This means that the free energy strength of the bonds that hold protein molecules together in the nucleus becomes nearly 9% larger above the transition temperature, when the aggregation rate is reduced.

In summary, the structural transition at Tc leads to an increase of free energy strength of the bonds that hold the protein molecules together in the protein nucleus, and to an increased entropy of the activated state. The result is a stabilization of the critical nuclei, that increase their radius and consequently decrease their number. The overall effect is to preserve the lens from the premature protein aggregation.

4.4.3 Effect of [Ca²⁺] and [α] and correlation between aggregation and nucleation rates

We have quantified the effect that Ca^{2+} and α-crystallin concentration have on the nucleation-aggregation kinetics.

In figure 24a and 24b K_N, K_A and R_C were reported in function of the $[Ca^{2+}]$, above and below *Tc*.

For *T>Tc* (figure 24a), if we increase $[Ca^{2+}]$, both rate constants raise their value till a saturation value, around $[Ca^{2+}]$=16 mM. The radii R_C are nearly constant and their value is ~28 nm, which is the same already reported in fig.22 for *T>Tc*. For *T<Tc* (figure 24b), both rate constants reach a saturation value around a $[Ca^{2+}]$=32 mM. Also in this case the radii R_C are nearly constant and their value is ~23 nm, which is the same already reported in fig.22 for *T<Tc*.
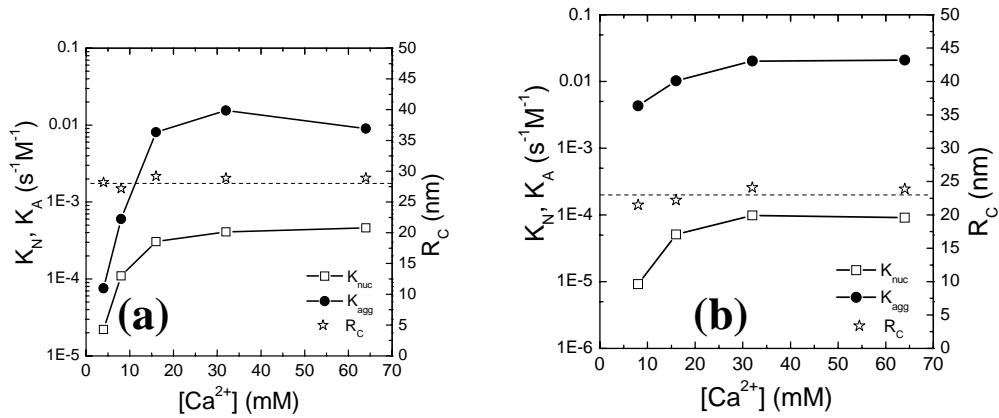

FIGURE 24 (a) Nucleation rates K_N (open squares), aggregation rates K_A (black circles) and critical radii *Rc* (stars) in function of $[Ca^{2+}]$ at T=325.54 K (b) Nucleation rates K_N (open squares), aggregation rates K_A (black circles) and critical radii *Rc* in function of $[Ca^{2+}]$ at T=314.45 K.

In figure 25, K_N and K_A are reported in function of [α] for T<Tc. The increase of [α] leads to an increase in both rate constants. Also in this case the radii R_C are nearly constant and their value is ~23 nm, which is the same already reported in fig.22 for *T<Tc*.
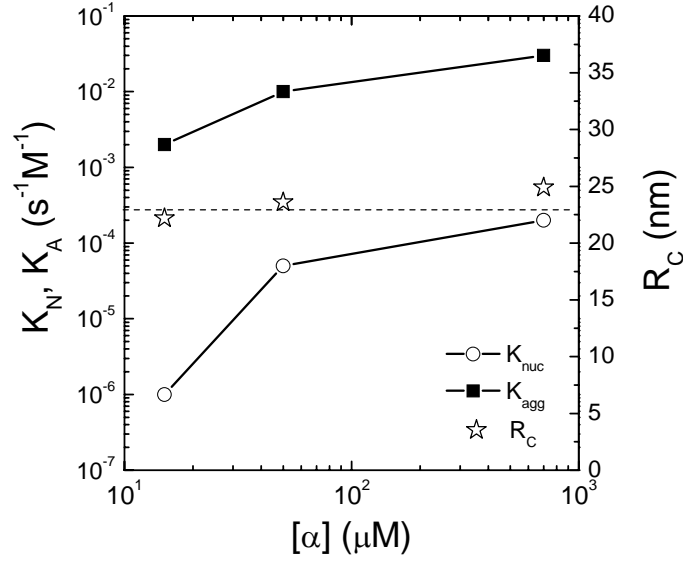
FIGURE 25 Nucleation rates K_N (open squares), aggregation rates K_A (black circles) and critical radii Rc (stars) in function of [α] at T=314.45 K

To get further insights about the effect of $[Ca^{2+}]$, [α] and T on the interaction potentials, it could be useful to compute from the rate constants the Fuchs stability ratios (eq.3.19), which are functionals of the total pairwise interaction potential of the monomers $(V_N(r))$ and of the nuclei $(V_A(r))$:

$$W_N = \Im\left(\frac{V_N(r)}{k_B T}\right)$$
$$W_A = \Im\left(\frac{V_A(r)}{k_B T}\right)$$

(4.26)

More the potential is repulsive, more stable is the protein suspension and higher is the Fuchs stability ratio (eq.3.18). In figure 26 we plotted W_A, the nucleus-nucleus stability ratio, versus W_N, the monomer-monomer stability ratio. We see that the stability ratios measured at different T, $[Ca^{2+}]$ and [α], lie on two different straight line in a log-log plot. It can be observed that all measurements performed at $T>Tc$ lie on the line with the higher slope, and those performed at $T<Tc$ lie on the other line. So we can establish a power law correlation between the ratios over and below Tc,

74

$$W_A \propto [W_N]^\eta \qquad (4.27)$$

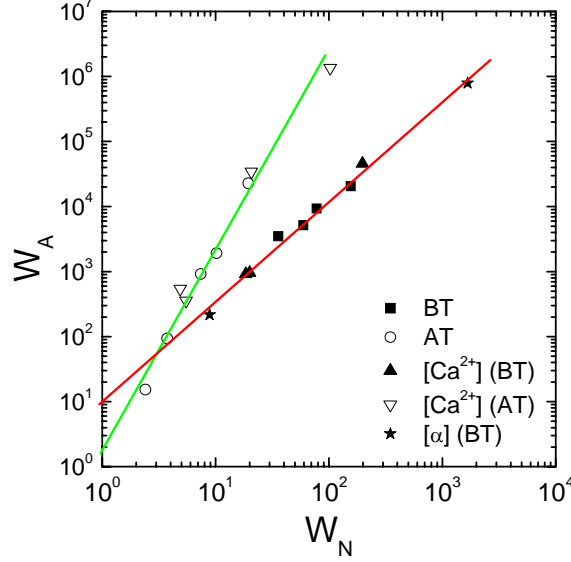For $T>Tc$ we find $\eta=3.00$ and for $T<Tc$ $\eta=1.53$.

FIGURE 26 Log-log plot of W_A, the nucleus-nucleus Fuchs stability ratio, versus W_N. the monomer-monomer Fuchs stability ratio. Black squares correspond to stability ratios measured at $T<Tc$ with [Ca2+]=16 mM and [α]=50 μM. Open circles correspond to stability ratios measured at different $T>Tc$ with [Ca2+]=16 mM and [α]=50 μM. Black triangles correspond to stability ratios measured at $T=314.45<$ Tc at different [Ca2+]. Open inverted triangles correspond to stability ratios measured at $T=325.28>(Tc)$ at different [Ca2+]. Black stars correspond to stability ratios measured at $T=314.45(<Tc)$ at different [α]. Solid lines are power fits to the data acquired below and over Tc.

These correlations between the stability ratios let us establish a correlation between the total pairwise interaction potential of the monomers ($V_N(r)$) and of the nuclei ($V_A(r)$) via the (4.26): the exponent η, which characterizes the power law correlation between the functionals of the interaction potentials, may depend from the structural arrangement of monomers in the nuclei, and in our case directly from Rc, because the monomers are arranged in a spherical assembly. Indeed at $T< Tc$, where Rc is ~23 nm, we find the exponent $\eta=1.53$. At $T>Tc$, where Rc is ~28 nm, the exponent becomes $\eta=3.00$.

Furthermore the correlations between the stability ratios over and below Tc let us get more insights about the effect of T, [Ca^{2+}] and [α] on the overall

process of nucleation and aggregation. We see that if we change $[Ca^{2+}]$ or $[\alpha]$ or T without crossing Tc, the correlation between the stability ratios is preserved. Indeed, as we already observed in this paragraph, variations in $[Ca^{2+}]$ and $[\alpha]$ don't alter the values of Rc.

These findings mean that the two step process, which is characterized in the nucleation-aggregation model by three parameters, actually can be characterized only by the exponent η which accounts either for the relations between the interaction potentials, either for the structural arrangement of the monomers in the nuclei.

5.Conclusions

The condensation of eye lens proteins is the main cause for lens opacification. Characterization of the aggregation kinetics is therefore an important tool that allows to distinguish between the several molecular mechanisms leading to protein aggregation. A kinetic model of the process that leads to the condensation of eye lens proteins into randomly distributed aggregates was exposed in this work. The model describes the growth kinetics as a two step-process, a nucleation phase followed by an aggregation phase. The quantitative modeling of the nucleation and aggregation kinetics by means of population balance equations (PBE) in protein dispersions was combined with an extensive experimental investigation using light scattering in order to compute experimentally measured quantities. The detailed comparison of the quantities computed from the PBE with the light scattering measurements allowed to identify the rate constants and the critical size of nucleus suitable for the description of nucleation and aggregation kinetics. The determination of both the nucleation rate and the critical radius allows for the indirect measurement of interfacial tension relevant in the characterization of the nucleation process.

The free energies associated with the activation processes are obtained from the rate constants. At the transition temperature Tc there is an increase in the free energies of activation with temperature, $\Delta\Delta G = \Delta G^{AT} - \Delta G^{BT}$, that is 1.1 Kcal/mol for the nucleation process and 8.2 Kcal/mol for the aggregation process. Therefore the probability that an activated state occurs in the nucleation process is nearly the same above and below Tc, whereas the probability that an activated state occurs in the aggregation process switches from $\exp(\Delta G/RT) \approx 10^{-5}$ to $\exp(\Delta G/RT) \approx 10^{-11}$ at Tc.

The quaternary structural transition of α-crystallin is also accompanied by an increase in the dimensions of the critical nuclei, and by a decrease of their number. Furthermore, we've also estimated an increase of the free energy strength of the bonds that hold the protein molecules together in the protein nucleus, to be nearly 9% larger above the transition temperature, when the aggregation rate is reduced. The overall result is the formation of a lesser number of larger and more stable critical nuclei.

Therefore, the α-crystallin above Tc exhibits a delay in the aggregation phase due to the simultaneous increase of the free energy of activation of the process and to a decrease of the number of critical nuclei. This effect preserves the lens from a premature opacification in such hypertermic and stressful conditions, and can be related to the temperature dependent chaperone effect of the α-crystallin already observed in literature (Raman and Rao, 1997).

According to our findings, we propose a possible mechanism of the exhibited heat-induced effect. The structural transition at Tc leads to an increase of free energy strength of the bonds that hold protein molecules together in the critical nucleus. This is probably related to an exposure of β-sheet regions observed over Tc (Walsh, 1991; Raman and Rao, 1997). The result is a stabilization of the critical nuclei, which increase their radius and decrease their number. The overall increase above Tc of the free energy of activation comes from two factors: the stabilization of the critical nuclei, which may contribute to

the increase in the activation energy of aggregation, and the release of water bound molecules and the unfolding of proteins that may contribute to the increased entropy of the activated state. Indeed, it is likely that a transition from more ordered, bound structure, to a more disordered, loose structure is the essence of the activation process preceding the formation of the dimers. The structural transition, therefore, may be the main cause of the delay in the aggregation process. The methodology developed and the determination of thermodynamics quantities as the free energy of activation, related to the kinetics process, can be used to evaluate the potential aggregation inhibitors or enhancers by the decrease or increase in the free energy of activation rates that they introduce.

Furthermore we've find two power law correlations between the Fuchs functionals of the total pairwise interaction potential of the monomers ($V_N(r)$) and of the nuclei ($V_A(r)$) over and below *Tc*: the exponent η characterizing these correlations may depend directly from the critical radius *Rc*. Indeed at *T< Tc*, where *Rc* is ~23 nm, we find the exponent η=1.53, and at *T>Tc*, where *Rc* is ~28 nm, the exponent becomes η=3.00. We've also seen that variations of [Ca^{2+}], [α] or *T* (without crossing *Tc*), preserve the correlation between the stability ratios. Indeed, as we already observed in this paragraph, variations in [Ca^{2+}] and [α] don't alter the values of *Rc* and therefore the structural arrangement of the monomers in the nuclei. These findings mean that the two step process, which is characterized by three parameters, actually can be characterized only by the exponent η which accounts for the relations between the interaction potentials and for the structural arrangement of the monomers in the nuclei.

In summary, from kinetic studies we had further evidence that cataract can be considered among the protein misfolding diseases, and furthermore that condensation of misfolded proteins does lead also to randomly distributed aggregates, and not only to fibrillization, through a nucleation mechanism. This

means that nucleation, rather than fibrillization, is a common feature of the misfolding diseases. The investigation on the protective mechanism towards the aggregation, related to a self-chaperone effect, strengthens the main hypothesis about the development of cataract, that, as lenticular proteins unfold with ageing, the chaperone capacity of α−crystallin will be exhausted and protein aggregates will be formed (Horwitz, 1992; Derham and Harding, 1999; Clark and Muchowski, 2000). In our opinion, the chaperone capacity may consist in the formation of more stable nuclei in stressful conditions, that delay, but do not stop, the aggregation process. With time, if the lens cell is repeatedly insulted by external agents, the number of this nuclei becomes larger, and because they are in a metastable state, their subsequent aggregation is inevitable and leads to cataract. This is coherent with the observation that the HMW forms of α-crystallin in the lens increase with age (Horwitz, 2003).

Further experiments are needed to confirm the mechanism of the temperature-dependent self-chaperone effect, and to detect it on other proteins and protein complexes. The finding of an exponent that can account either for the relations between the interaction potentials of nucleation and aggregation, either for the structural arrangement of the monomers in the nuclei, needs to be further investigated on model systems and on other protein suspensions. *In vivo* investigations are also needed to determine whether the citotoxicity comes from nucleating or aggregating species and to subsequently test properties of nucleation or aggregation inhibitors able to contrast these diseases.

Bibliography

Anderson V. and H. Lekkerkerker, "Insights into phase transition kinetics from colloid science", Nature **416**, 811 (2002).

Andreasi Bassi F. Giuseppe Arcovito, Marco De Spirito, Alvaro Mordente, and Giuseppe E. Martorana "Self-Similarity Properties of α-Crystallin Supramolecular Aggregates" Biophysical Journal, Volume 69, 2720-2727 (1995).

Axford S., "Aggregation of Colloidal Silica: Reaction-Limited Kernel, Stability Ratio and Distribution Moments", J. Chem. Soc., Faraday Trans. 93, 303 (1997).

Ball R., D. Weitz, T. Witten, and F. Leyvraz, "Universal Kinetics in Reaction-Limited Aggregation", Phys. Rev. Lett. 58, 274 (1987).

Bassnett, S., Lens organelle degradation. Exp. Eye Res. 74, 1–6 (2002).

Behrens S., D. Christl, R. Emmerzael, P. Schurtenberger, and M. Borkovec, « Charging and Aggregation Properties of Carboxyl Latex Particles: Experiments versus DLVO Theory », Langmuir 16, 2566 (2000).

Benedek, G.B., "Theory of transparency of the eye". Appl. Opt. 10, 459–473 (1971).

Benedek, G.B., Clark, I.J., Serrallach, E.N., Young, C.Y., Mengel, L., Sauke, T., Bagg, A., Benedek, K., "Light scattering and reversible cataracts in the calf and human lens" Philos. Trans. R. Soc. London A293, 329–340(1979).

Benedek, G.B., "Cataract as a protein condensation disease: the proctor lecture" Invest. Ophthalmol. Vis. Sci. 38, 1911–1921 (1997).

Berne B. and R. Pecora, *Dynamic Light Scattering*, Wiley, New York, (1976).

Bitan, G., A. Lomakin, and D. B. Teplow.. Amyloid-b-protein oligomerization: prenucleation interactions revealed by photo-induced cross-linking of unmodified proteins. J. Biol. Chem. 276:35176–35184. (2001)

Berbers, G.A., Hoekman, W.A., Bloemendal, H., de Jong, W.W., Kleinschmidt, T., Bloemendal, H., de Jong, W.W., "Lens proteins and their genes". Prog. Nucleic Acid Res. Mol. Biol. 41, 259–281(1991).

Blundell, T.L., Lindley, P., Miller, L., Moss, D., Slingsby, C., Tickley, I., Turnell, B., Wistow, G., "The molecular structure and stability of the eye lens: X-ray analysis of gamma-crystallin II". Nature 289, 771–777 (1981).

Bostrom M., D. Williams, and B. Ninham, "Specific Ion Effects: Why DLVO Theory Fails forBiology and Colloid Systems", Phys. Rev. Lett. **87**, 168103 (2001).

Braunitzer, G., . "Homology between the primary structures of the major bovine beta-crystallin chains" Eur. J. Biochem. 139, 467–479 (1984).

Broide M. and R. Cohen, Experimental Evidence of Dynamic Scaling in Colloidal Aggregation, Phys. Rev. Lett. 64, 2026 (1990).

Bron, A.J., Vrensen, G.F., Koretz, J., Maraini, G., Harding, J.J., "The ageing lens. Ophthalmologica" 214, 86–104 (2000).

Brown W., "Light Scattering. Principles and Development", Clarendon Press, Oxford, (1996).

Butte A., G. Storti, and M. Morbidelli, "Evaluation of the Chain Length Distribution in Free-Radical Polymerization-1", Macromol. Theory Simul. 11, 22 (2002).

Carrell, R. W. & Lomas, D. A. Conformational disease.*Lancet* 350, 134–138 (1997).

Chayen N E Curr. Opin. Struct. Bio. 14 577 (2004).

Chen, S. H., and J. Teixeira. "Structure and fractal dimension of protein-detergent complexes" Phys. Rev. Lett. 57:2583-2586 (1986).

Clark, J.I., Muchowski, P.J., . "Small heat-shock proteins and their potential role in human disease" Curr. Opin.Struct. Biol. 10, 52–59 (2000).

Collins, S. R., A. Douglass, R. D. Vale, and J. S. Weissman. "Mechanism of prion propagation: amyloid growth occurs by monomer addition" PLoS Biol. 2:1582–1590 (2004).

Csermely, P., "Chaperone overload is a possible contributor to 'civilization diseases'". Trends Genet. 17, 701–704 (2001).

Debenedetti P G "Metastable Liquids" Princeton University Press, Princeton, (1996).

de Hoog E., W. Kegel, A. van Blaaderen, and H. N. W. Lekkerkerker, "Direct observation of crystallization and aggregation in a phase-separating colloid-polymer suspension", Phys. Rev.E **64**, 021407 (2001).

de Jong, W.W., Caspers, G.-J., Leunissen, J.A.M., . "Genealogy of the alpha-crystallin–small heat-shock protein superfamily". Int. J. Biol. Macromol. 22, 151–162 (1998).

Delaye, M., J. I. Clark, and G. B. Benedek.." Identification of the scattering elements responsible for lens opacification in cold cataracts".Biophys. J. 37:647-656 (1982).

del Valle L. J., Cristina Escribano, Juan J. Perez, Pere Garriga "Calcium-induced decrease of the thermal stability and chaperone activity of α-crystallin" Biochimica et Biophysica Acta 1601 100– 109 (2002).

Derham, B.K., Harding, J.J., "Alpha-crystallin as a molecular chaperone". Prog. Retin. Eye Res. 18, 463–509 (1999).

Derjaguin, B. *"Theory of Stability of Colloids and Thin Films",* English Translation, Consultants Bureau, New York and London (1989).

Dobson, C.M., "Protein misfolding, evolution and disease". Trends Biochem. Sci. 24, 329–332 (1999).

Doss-Pepe, E.W., Carew, E.L., Koretz, J.F., "Studies of the denaturation patterns of bovine alpha-crystallin using an ionic denaturant, guanidine hydrochloride and a non-ionic denaturant, urea". Exp. Eye Res. 67, 657–679 (1998).

Duncan G., T.J. Jacob, "Human cataract formation", in: J. Nugent, J.Whelan (Eds.), Ciba Foundation Symposium, vol. 106, Pitman Press, London, pp. 132–152 (1984).

Duncan G., R. van Heyningen, Exp. Eye Res. 25 183– 193 (1977).

Durand D., J. Gimel, and T. Nicolai, "Aggregation, gelation and phase separation of heat denaturated globular proteins", Physica A **304**, 253 (2002).

Evans, K. C., E. P. Berger, C. Cho, K. H. Weisgraber, and P. T. Lansbury Jr.. Apolipoprotein E is a kinetic but not a thermodynamic inhibitor of amyloid formation: implications for the pathogenesis and treatment of Alzheimer disease. Proc. Natl. Acad. Sci. USA. 92:763–767 (1995).

Family F., P. Meakin, and T. Vicsek, Cluster Size Distribution in Chemically Controlled Cluster-Cluster Aggregation, J. Chem. Phys. **83**, 4144 (1985).

Flyvbjerg, H., E. Jobs, and S. Leibler. "Kinetics of self-assembling microtubules: an ''inverse problem'' in biochemistry. Proc. Natl.Acad. Sci. USA. 93:5975–5979 (1996).

Forrest S. and T. Witten, Long-Range Correlations in Smoke-Particle Aggregates, J. Phys. A- Math. Gen. **12**, L109 (1979).

Forsythe G.E., Michael A. Malcolm, and Cleve B. Moler. *"Computer Methods for Mathematical Computations"*. Englewood Cliffs, NJ: Prentice-Hall (1977).

Fuchs, N., ¨Uber die Stabilit¨at und Au_adung der Aerosole, Z. Phys. **89**, 736.743 (1934).

Garcia-Ruiz J M J. Struct. Biol. 142 22 (2003)

Gorti S, Forsythe E L, and Pusey M L Crys. Growth Design 5 47 (2004).

Grainger, R.M., "Embryonic lens induction: shedding light on vertebrate tissue determination". Trends Genet.8, 349–355 (1992).

Herbrink, P., van Westreenen, H., Bloemendal, H., . „Further studies on the polypeptide chains of beta-crystallin". Exp. Eye Res. 20, 541–548(1975).

Horwitz, J., . "Alpha-crystallin can function as a molecular chaperone". Proc. Natl. Acad. Sci. USA 89, 10449–10453 (1992).

Horwitz, J., . "Alpha-crystallin". Exp. Eye Res. 76, 145–153 (2003).

Hughes, A., . Seeing cones in living eyes. Nature 380, 393–394 (1996).

Iwaki, T., Kume-I

waki, A., Goldman, J.E., . „Cellular distribution of alpha B-crystallin in non-lenticular tissues". J. Histochem. Cytochem. 38, 31–39.(1990)

Jarrett, J. T., Berger, E. P. & Lansbury, P. T. Jr. „The C-terminus of the β protein is critical in amyloidogenesis". *Ann. NY Acad. Sci.* **695**, 144–148 (1993).

Jedziniak J.A., J.H. Kinoshita, E.M. Yates, L.O. Hocker, G.B. Benedek, Invest. Ophthalmol. 11 905– 915. (1972)

Jedziniak J.A., J.H. Kinoshita, E.M. Yates, L.O. Hocker, G.B. Benedek, Exp. Eye Res. 15 185– 192. (1973)

Jullien R., "The Application of Fractals to Colloidal Aggregation", Croat. Chem. Acta **65**, 215 (1992).

Kayed, R., E. Head, J. L. Thompson, T. M. McIntire, S. C. Milton, C. W. Cotman, and C. G. Glabe.. "Common structure of soluble amyloid oligomers implies common mechanism of pathogenesis".Science. 5618:486–489.(2003)

Kerker M., *"The Scattering of Light and other electromagnetic radiations"*, Academic Press (1969).

Khurana, R., C. Ionescu-Zanetti, M. Pope, J. Li, L. Nielson, M. Ramı´rez-Alvarado, L. Regan, A. Fink L., and S. A. Cartery.. "A general model for amyloid fibril assembly based on morphological studies using atomic force microscopy". Biophys. J. 85:1135–1144.(2003)

Kinjo, A.R., Takada, s., "Competition between protein folding and aggregation with molecular chaperones in crowded solutions:insights from mesoscopic simulations", Biophys Journ 85, 3521-3531(2003)

Klein R. and B. D'Aguanno, "Static scattering properties of colloidal suspensions", in *Light Scattering. Principles and Development*, edited by W. Brown, page 30, Clarendon Press, Oxford,

(1996).

Koppel, D. E.. "Analysis of macromolecular polydispersity in intensity correlation spectroscopy: the method of cumulants". J. Chem. Phys.57:4814-4820.(1972)

Krall A. and D. Weitz, "Internal Dynamics and Elasticity of Fractal Colloidal Gels", Phys. Rev. Lett. **80**, 778 (1998).

Lasaga, kinetic theory, Princeton university press (1998)

Lashuel, H. A., and P. T. Lansbury, Jr. "Are amyloid diseases caused by protein aggregates that mimic bacterial pore-formingtoxins?" Quarterly Reviews of Biophysics, Cambridge University Press, Cambridge, UK.(2006)

Lattuada M. Hua Wu, and Massimo Morbidelli "Hydrodynamic radius of fractal clusters" Journal of Colloid and Interface Science 268 96–105 (2003)

Lin M., H. Lindsay, D. Weitz, R. Ball, R. Klein, and P. Meakin, "Universality in colloid aggregation", Nature **339**, 360 (1989).

Lin M., H. Lindsay, D. Weitz, R. Ball, R. Klein, and P. Meakin, "Universality of fractal aggregates as probed by light scattering", Proc. R. Soc. Lond. A **423**, 71 (1989).

Lin M., H. Lindsay, D. Weitz, R. Klein, R. Ball, and P. Meakin [21], "Universal Reaction-Limited Aggregation", Phys. Rev. A **41**, 2005 (1990).

Lin M., H. Lindsay, D. Weitz, R. Ball, R. Klein, and P. Meakin, "Universal Diffusion-Limited Aggregation", J. Phys.: Condens. Matter **2**, 3093 (1990).

Linder P. and T. Zemb, *Neutrons, X-rays and Light: Scattering Methods Applied to Soft Condensed Matter*, Elsevier Science B.V., Amsterdam, (2002).

Lomakin, A., D. B. Teplow, D. A. Kirschner, and G. B. Benedek. "Kinetic theory of fibrillogenesis of amyloid-protein". Proc. Natl.Acad. Sci. USA. 94:7942–7947.(1997)

Ma, Z.X., Hanson, S.R.A., Lampi, K.J., David, L.L., Smith, D.L., Smith, J.B., . "Age-related changes in human lens crystallins identified by HPLC and mass spectrometry". Exp. Eye. Res. 67, 21–30.(1998)

MacRae, T.H., "Structure and function of small heat shock/alpha-crystallin proteins: established concepts and emerging ideas". Cell. Mol. Life Sci. 57, 899–913.(2000)

Mandelbrot, B. *The Fractal Geometry of Nature*, W. H. Freeman, San Francisco, (1982).

Maulucci G, De Spirito M, Arcovito G, Boffi F, Castellano AC, Briganti G "Particle size distribution in DMPC vesicles solutions undergoing different sonication times" Biophys J. May;88(5):3545-50. 2005 Feb 4. (2005)

Melis S., M. Verduyn, G. Storti, M. Morbidelli, and J. Baldyga, "Effect of Fluid Motion on the Aggregation of Small Particles Subject to Interaction Forces", AIChE Journal **45**, 1383 (1999).

Michael, R., van Marle, J., Vrensen, G.F., van den Berg, T.J., "Changes in the refractive index of lens fibre membranes during maturation—impact on lens transparency". Exp. Eye Res. 77, 93–99 (2003).

Minton, A.P., Implications of macromolecular crowding for protein assembly. Curr.Op.Struct. Bio. (2000), 10: 34-39.

Mornon, J.P., Halaby, D., Malfois, M., Durand, P., Callebaut, I., Tardieu, A., Alpha-Crystallin C-terminal domain: on the track of an ig fold. Int. J. Biol. Macromol. 22, 219–227(1998).

Nielsen, L. R., R. Khurana, A. Coats, S. Frokjaer, J. Brange, S. Vyas, V. N. Uversky, and A. L. Fink.. Effect of environmental factors on the kinetics of insulin fibril formation: elucidation of the molecular mechanism. Biochemistry. 40:6036–6046.(2001)

Odriozola G., A. Schmitt, J. Callejas-Fernandez, R. Martinez-Garcia, and R. Hidalgo-Alvarez, Dynamic Scaling Concepts Applied to Numerical Solutions of Smoluchowski's Rate Equation, J. Chem. Phys. **111**, 7657 (1999).

Oxtoby D W J. Phys. Cond. Matt. 4 7627(1992)

Oxtoby D W Acc. Chem. Res. 31 91(1998)

Padrick, S. B., and A. D. Miranker.. "Islet amyloid: phase partitioning and secondary nucleation are central to the mechanism of firillogenesis". Biochemistry. 41:4694–4703.(2002)

Pasternack, R. F., E. J. Gibbs, S. Sibley, L. Woodard, P. Hutchinson, J.Genereux, and K. Kristian.. "Formation kinetics of insulin-basedamyloid gels and the effect of added metalloporphyrins". Biophys. J.90:1033–1042.(2006)

Peula J., R. Santos, J. Forcada, R. Hidalgo-Alvarez, and F. de las Nieves, "Study on the Colloidal Stability Mechanisms of Acetal-Functionalized Latexes", Langmuir **14**, 6377 (1998).

Porcel R., A. Jodar, A. Cabrerizo, R. Hidalgo-Alvarez, and A. Martin-Rodriguez, "Sequential Adsorption of Triton X-100 and Sodium Dodecyl Sulfate onto Positively and Negatively Charged Polystyrene Latexes", J. Colloid Interface Sci. **239**, 568 (2001).

Pusey P., J. Rarity, R. Klein, and D. Weitz, "Comment on Hydrodynamic Behavior of Fractal Aggregates"., Phys. Rev. Lett. **59**, 2122 (1987).

Putilina, T., Skouri-Panet, F., Prat, K., Lubsen, N.H., Tardieu, A., . « Subunit exchange demonstrates a differential chaperone activity of calf alpha-crystallin towards betaLOW- and individual gamma-crystallins". J. Biol. Chem. 278, 13747–13756.(2003)

Rajini B., P. Shridas, C. Sivakama-Sundari, D. Muralidhar, S.Chandani, F. Thomas, Y. Sharma, J. Biol. Chem. 276 38464– 38471.(2001)

Raman B.and Rao C.R. "Chaperone-like Activity and Temperature-induced Structural Changes of a-Crystallin" PNAS Vol. 280, No. 23, Issue of June 10, pp. 21726–21730, (2005)

Ramkrishna D., B. Shah, and J. Borwanker, "Analysis of Population Balance-III", Chem. Eng. Sci. **31**, 435 (1976).

Ramkrishna, D**.**, *Population Balances*, Academic Press, San Diego, (2000).

Romero-Cano M., A. Martin-Rodriguez, G. Chauveteau, and F. de las Nieves, "Colloidal Stabilization of Polystyrene Particles by Adsorption of Nonionic Surfactants I. Adsorption Study", J. Colloid Interface Sci. **198**, 266 (1998).

Romero-Cano M, A. Martin-Rodriguez, G. Chauveteau, and F. de las Nieves, "Colloidal Stabilization of Polystyrene Particles by Adsorption of Nonionic Surfactants II. Electrosteric Stability Studies", J. Colloid Interface Sci. **198**, 273 (1998).

Romero-Cano M., A. Martin-Rodriguez, and F. de las Nieves, "Electrosteric Stabilization of Polymer Colloids with Different Functionality", Langmuir **17**, 3505 (2001).

Russel W., D. Saville, andW. Schowalter, *"Colloidal Dispersions"*, Cambridge University Press, Cambridge, UK, (1989).

Sampson K. and D. Ramkrishna, "Particle Size Correlations and the Effects of Limited Mixing on Agglomerating Particulate Systems", J. Colloid Interface Sci. **104**, 269 (1985).

Santini, S. A., A. Mordente, E. Meucci, G. A. D. Miggiano, and G. E. Martorana. (1992). "Conformational stability of a-crystallin. Evidence for the destabilizing effect of ascorbate". Biochem. J. 287:107-112.

Scheffold F. and P. Schurtenberger, "Light Scattering Probes of Viscoelastic Fluids and Solids,
Soft Materials" **1**, 139 (2003).

Scheibel, T., J. Bloom, and S. L. Lindquist. 2004. "The elongation of yeast prion fibers involves separable steps of association and conversion" .Proc. Natl. Acad. Sci. USA. 101:2287–2292.

Scherzinger, E. *et al.* "Self-assembly of polyglutamine containing huntingtin fragments into amyloid-like fibrils:implications for Huntington's disease pathology". *Proc. Natl Acad. Sci. USA* **96**, 4604–4609 (1999).

Selkoe, D. J.. "Cell biology of protein misfolding: the examples of Alzheimer's and Parkinson's diseases". Nat. Cell Biol. 6:1054–1061. (2004)

Sefcik J., M. Verduyn, G. Storti, and M. Morbidelli, "Charging of Latex Particles Stabilized by Sulfate Surfactant", Langmuir **19**, 4778 (2003).

Seinfeld, J. H., and S. N. Pandis. "Atmospheric Chemistry and Physics". John Wiley and Sons, New York. (2005)

Shoghi-Jadid, K., J. R. Barrio, V. Kepe, H. M. Wu, G. W. Small, M. E.Phelps, and S. C. Huang.. "Imaging b-amyloid fibrils in Alzheimer's disease: a critical analysis through simulation of amyloid fibril polymerization". Nucl. Med. Biol. 32:337–351.(2005)

Sipe, J. D.. Amyloid Protein: "The Beta Sheet Conformation and Disease". John Wiley and Sons, New York.(2005)

Slusky, V., J. A. Tamada, A. M. Klibanov, and R. Langer. "Kinetics of insulin aggregation in aqueous solutions upon agitation in the presence of hydrophobic surfaces". Proc. Natl. Acad. Sci. USA. 88:9377–9381(1991)

Sorensen C. and G. Roberts, "The Prefactor of Fractal Aggregates", J. Colloid Interface Sci. **186**, 447 (1997).

Sorensen C. and G.Wang, "Size Distribution Effect on the Power Law Regime of the Structure Factor of Fractal Aggregates", Phys. Rev. E **60**, 7143 (1999).

Sorensen C., "Light Scattering by Fractal Aggregates: A Review", Aerosol Sci. Tech. **35**, 648 (2001).

Soto, C. "Protein misfolding and disease; protein refoldingand therapy". *FEBS Lett.* 498, 204–207 (2001).

Srinivasan, A.N., Nagineni, C.N., Bhat, S.P., . "Alpha A-crystallin is expressed in non-ocular tissues". J. Biol. Chem.267, 23337–23341.(1992)

Tardieu, A., Laporte, D., Licinio, P., Krop, B., Delaye, M., . « Calf lens alpha-crystallin quaternary structure. A three-layer tetrahedral model". J. Mol. Biol. 192, 711–724. (1986)

Teplow, D. B. "Structural and kinetic features of amyloid β-protein fibrillogenesis". *Amyloid* **5**, 121–142 (1998).

Thorn M. and M. Seesselberg, "Dynamic Scaling in Colloidal Aggregation: Comparison of Experimental Data with Results of Stochastic Simulations", Phys. Rev. Lett. **72**, 3622 (1994).

Tirado-Miranda M., A. Schmitt, J. Callejas-Fernandez, and A. Fernandez-Barbero, "The aggregation behavior of protein-coated colloidal particles: a light scattering study", Eur. Biophys. J. 32, 128 (2003).

Turnbull D and Vonnegut B 1952 Ind. Eng. Chem. 44 1292

Uversky, V. N., J. Li, and A. L. Fink. 2001. "Metal-triggered structural transformations, aggregation, and fibrillation of human α-synuclein". J. Biol. Chem. 276:44284–44296.

van Dongen P. and M. Ernst, "Cluster Size Distribution in Irreversible Aggregation at Large Times", J. Phys. A: Math. Gen. **18**, 2779 (1985).

van Dongen P. and M. Ernst, "Dynamic Scaling in the Kinetics of Clustering", Phys. Rev. Lett. 54, 1396 (1985).

van Montfort, R.L., Basha, E., Friedrich, K.L., Slingsby, C., Vierling, E., . "Crystal structure and assembly of a eukaryotic small heat shock protein". Nat. Struct. Biol. 8, 1025–1030. (2001)

von Smoluchowski M., „Versuch einer mathematischen Theorie der Koagulationskinetik kolloider L¨osungen", Z. Phys. Chem. **92**, 129 (1917).

Vervwey E. and J. Overbeek, *Theory of the Stability of Lyophobic Colloids*, Elsevier Publishing Co., New York, (1948).

Walsh, M. T., Asok C. Sens, and Bireswar Chakrabarti II "Micellar Subunit Assembly in a Three-layer Model of Oligomeric a-Crystallin" JBC Vol *266,* No. 30, Issue of October ' 25, PP, 20079-20084.(1991)

Weijers M., R. Visschers, and T. Nicolai, "Light Scattering Study of Heat-Induced Aggregation and Gelation of Ovalbumin", Macromolecules **35**, 4753 (2002).

Wiltzius P., "Hydrodynamic Behavior of Fractal Aggregates", Phys. Rev. Lett. **58**, 710 (1987).

Witten T. and L. Sander, "Diffusion-Limited Aggregation, a Kinetic Critical Phenomenon", Phys. Rev. Lett. **47**, 1400 (1981).

Wood, S. J. *et al.* "α-Synuclein fibrillogenesis is nucleation dependent.Implications for the pathogenesis of Parkinson's disease". *J. Biol. Chem.* **274**, 19509–19512 (1999).

Zhu P. and D. Napper, "Studies of aggregation kinetics of polystyrene latices sterically stabilized by poly(N-isopropylacrylamide)", Phys. Rev. E **50**, 1360.1366 (1994).